

1 **Light detection system simulations for SBND**

2 D. Garcia-Gamez, W. Foreman, A. Hackenburg, C. Hill, P. Kryczynski, A. M. Szelc

3 **Abstract**

4 Detection of scintillation light can play several important roles in LArTPCs. Increased
5 collection efficiency could result in the improvement of time, energy, and position resolution.
6 We have developed a detailed MC simulation to study the performance of different types of
7 light systems in SBND using the LArSoft framework. Due to the vast number of photons
8 typically produced in neutrino physics events, a full optical simulation becomes extremely
9 hard to run on reasonable time scales. We present the results for two possible light detection
10 systems: (i) a traditional TPB-coated PMT based system and (ii) a system based on TPB-
11 coated reflector foils.

12 **1 Introduction**

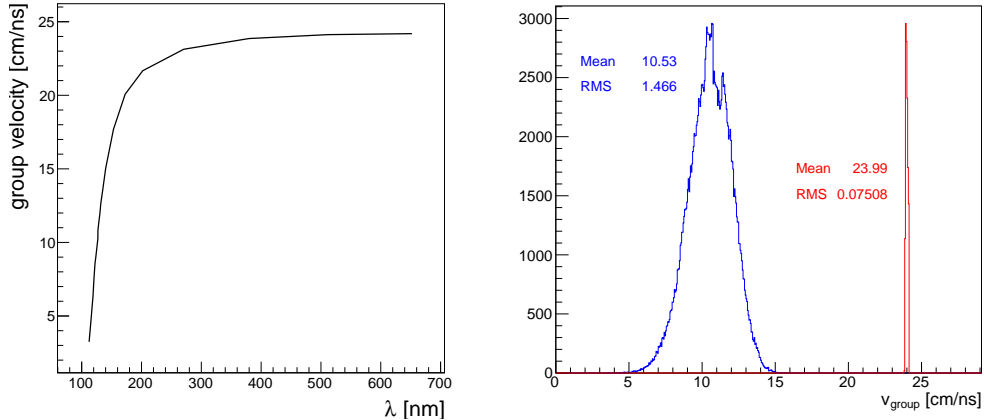


Figure 1: (Left) Group velocity of the photons in liquid argon as a function of their wavelengths. (Right) Group velocity distributions for the VUV scintillation photons produced in the liquid argon (blue) and the TPB-reemitted visible component (red).

13 Liquid argon is a prolific scintillator emitting on the order of forty thousand photons per
14 MeV of deposited energy. These photons carry information complementary to the ionisation
15 normally read out in LArTPCs. In the most basic scheme the scintillation photons are
16 used as a trigger for non-beam events and to reconstruct their position in the coordinates
17 spanning from the anode wires to the cathode also called the drift. This by itself allows
18 a much more precise reconstruction of the energy of these events given that charge can be
19 attenuated during drifting which can be corrected for only if the original position is known.

Liquid argon scintillation light has the potential to enhance the capabilities of the LArTPC performance in many more ways.

It is expected that scintillation light can also greatly improve the timing capabilities of LArTPC detectors, since its arrival time is on the order of nanoseconds even for large detectors. Although timing behaviour of liquid argon scintillation in conjunction with the emission spectra of wavelength shifters is well understood [1] and its effect on the arrival time can be corrected for, studies of second order transport effects like Rayleigh scattering, have not been carried out in full until now. An additional factor affecting timing resolution could be the width of the argon light emission peak, see Fig. 1 and the behaviour of the refractive index, which changes very steeply in the argon emission range. This can result in differences in group velocity as high as a factor of two between different VUV light photons and even larger between VUV and Visible. At lower wavelengths, visible light, the refractive index is close to one so the velocity increases and the variance decreases resulting in a smaller variation in the velocity.

Liquid argon scintillation light can also be used for energy reconstruction, as has been successfully demonstrated by liquid-argon dark matter experiments [2, 3]. This functionality requires a significant increase in light collection efficiency, and as such has not been exploited in neutrino detectors up to now. The energy emitted in scintillation light is complementary to that of charge, and collecting both could minimize effects from quenching which is a large source of uncertainties in LArTPCs.

Precise timing resolution could enable even 3D localization of the event position in the detector using only scintillation light, in addition to the 2D localization developed by MicroBooNE. The positional resolution in surface LArTPCs is necessary to reject cosmic ray muon tracks of which there can be as many as 5 per frame. The scintillation light arrives much faster than the drifted charge providing much more precise timing, so it can be used to determine whether an event occurred inside the beam window. Being able to reconstruct the y-z position of the event only based on the scintillation light only makes matching of the background events to light events possible. Adding the possibility of reconstruction in the third, x, coordinate could improve this capability even further.

SBND has the potential to determine how the enhanced energy, position and timing resolution in liquid argon detectors can be accomplished and used to enhance the physics programme. This note presents the results of studies performed with the LArSoft software package to study the advantages and capabilities of the high Light Yield (LY) Light Detection System (LDS) projected for SBND and the performance of its different variants. As of this writing, the studies have looked at a PMT only system with an opaque or transparent CPA, as well as a system with PMTs and Wavelength-shifter covered foils covering the CPA, and, for comparison, a setup with the whole inner chamber walls covered by foils.

The next section describes the SBND LDS variants implemented in the simulation, as well as the description of the particle samples used to determine the capabilities of the SBND LDS. This is followed by a brief description of how the simulation in LArSoft is performed, focusing on the improvements made for the SBND simulation. We then follow with a description of the studies of timing, energy and position resolution, finally closing with preliminary studies of effects of the high light yield events on the electronics.

2 Description of the simulated configurations

An important part of the mission of SBND is to be R&D for future LAr neutrino experiments. Its relatively small volume makes it an excellent test-bed for new light detection system designs. The LDS components under evaluation for SBND include traditional TPB-coated PMTs, TPB-coated reflector foils, and acrylic light guide bars read out at the ends with SiPMs. In this note we will focus on the two first components mentioned above.

TPB-coated PMTs. It has been demonstrated that a system based on TPB-coated cryogenic PMTs works well in modest-sized experiments (ICARUS [8], MicroBooNE [6]), but they are difficult to scale to bigger ones (like DUNE).

TPB-coated reflector foils. Adapted from liquid argon dark matter detectors, the installation of these foils inside the time projection chamber volume enhance light collection

74 without increasing the number of photodetectors. A similar system is currently implemented
 75 in the LArIAT experiment [9].

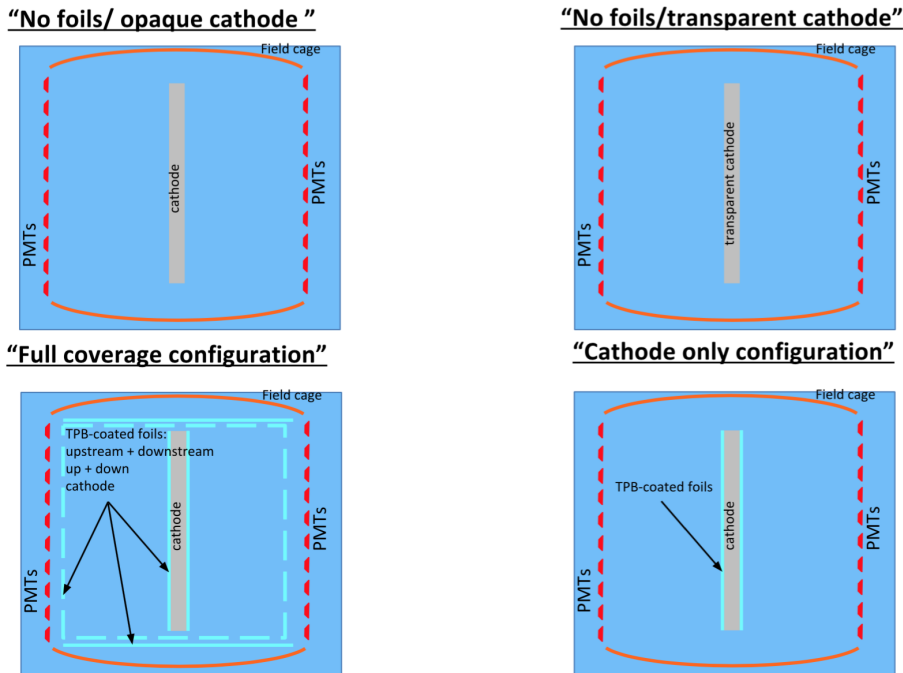
76 *2.1 Detector Configurations*

77 In this work we present the developed methods to benchmark these different components.
 78 In particular studying the effects of adding wavelength shifter covered reflector foils to an
 79 array of photomultipliers. For these studies we have simulated the four different geometry
 80 configurations shown in Figure 2.

81 **No foils opaque and transparent cathode.** In these configurations we have simulated
 82 the SBND geometry with and without the cathode. The positions of the 60 8" PMTs in
 83 the photocathode plane are shown in Figure 3. It tries to follow the current detector design
 84 of allocating five PMTs in each APA-frame window. By comparing the number of photons
 85 arriving to the different PMTs in these two configurations we will be able to emulate, in
 86 an effective way, the effect of a cathode with a certain (70% in our case) transparency (top
 87 panels in Figure 2).

88 **Cathode-only configuration.** In this configuration, the opaque cathode has been covered
 89 by a TPB-coated reflector foil, as the bottom right panel in Figure 2 shows.

90 **Full coverage configuration.** Now, TPB-coated reflector foils are covering the whole TPC
 91 active volume, as the bottom left panel in Figure 2 shows.



92 Figure 2: Pictures of the simulated configurations.

93 To compare the performance of the different configurations we will need to be able to
 94 distinguish between the direct and the reflected (TPB reemitted in the foils) light signals.
 95 Henceforth in the note, we will refer to both components as **VUV and visible** respectively,
 96 according to the wavelength they have when arriving to the PMT windows. Note that the
 97 VUV direct light, to be detected, will be wavelength shifted into visible by the TPB coating
 the PMT window, and reemitted with a forward efficiency of 50%.

98 *2.2 Particle samples used.*

99 To determine the capabilities of the SBND LDS options described above, we have simulated
 100 samples of muons and protons at different energies and topologies. Muons were chosen to
 101 study cosmic events, and protons because in most of the ν_e interactions in the liquid argon

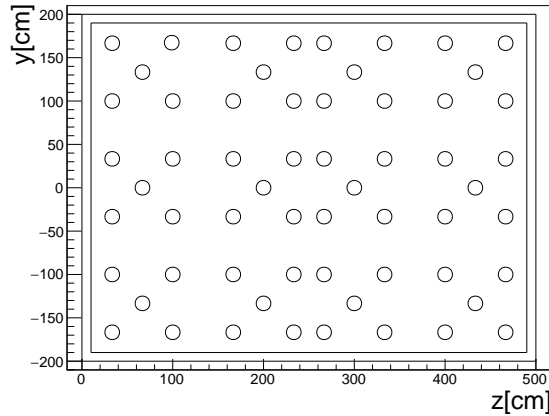


Figure 3: “Realistic” array of PMTs used in all the studies on this note.

Topology	(x, y, z) cm	θ°	ϕ°
muons (1)	(25, 200, 0)	-40 ± 10	0 ± 10
muons (2)	(100, 200, 0)	-40 ± 10	0 ± 10
muons (3)	(175, 200, 0)	-40 ± 10	0 ± 10
muons (4)	(100, 0, 0)	0 ± 10	0 ± 10
muons & protons (5)	(3, 0, 250)	0 ± 10	90 ± 10
muons & protons (6)	(100, 0, 250)	0 ± 10	30 ± 10
muons & protons (7)	(100, 0, 250)	0 ± 10	-30 ± 10
protons (8)	(50, 0, 250)	0 ± 10	0 ± 10
protons (9)	(150, 0, 250)	0 ± 10	0 ± 10
protons (10)	(x, 0, 250)	0 ± 10	0 ± 10
protons (11)	(100, 0, 250)	0 ± 180	0 ± 180

Table 1: Initial conditions of the sample of particles generated for this study. Most of these topologies are shown in Figure 4. In topology (10) $x = 5, 45, 85, 125, 145, 185$ cm to cover with more detail the different distances to the photocathode. Topology (11) was generated for the positioning study shown in Figure 19.

at least one proton is produced. Figure 4 illustrates the different samples, where the (x/drift, y/height, z/length) coordinates of the injection point for each topology, together with the central values of their polar (θ) and azimuth (ϕ) angles are indicated. All these angles vary within a certain window when we define the direction of the particles in our simulations (see Table 1 for full details). For each topology and particle we have simulated ~ 1500 events with $E = 100, 200, 300, 500, 1000, 1500$ MeV for the muons and $E = 20, 50, 100, 200, 300, 400, 500$ MeV for the protons. The statistics generated in the case of topology 11 was a factor 10 (15000 events) larger than the others, to ensure enough events in all directions.

From now on in the note, in all the studies carried out using our sample of simulated protons described above, we have applied trigger conditions in our events. The trigger strategies have been designed to avoid dealing with a large quantity of spurious ^{39}Ar and Radon backgrounds, despite the large Light Yield of our different configurations [11]. In particular, an event will be triggering our LDS if we have at least three PMTs each with at least three (five) photoelectrons arriving in the first 100 ns for the case of the “cathode only” and the 70% transparent cathode (“full coverage”) configurations.

3 Optical simulation in LArSoft

SBND simulations are performed within the open source LArSoft framework, which provides simulation reconstruction and analysis tools for current and future LAr TPC experiments.

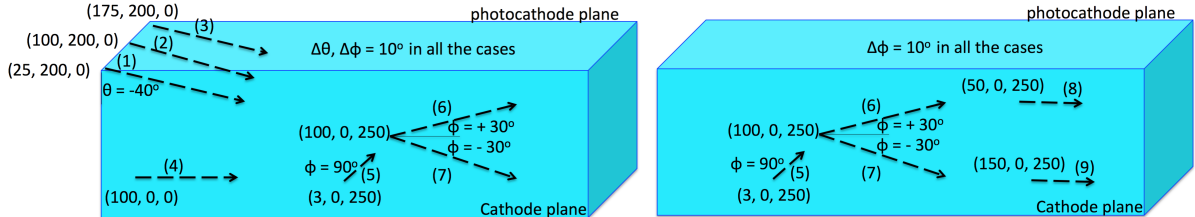


Figure 4: Picture of the different topologies we have simulated for our sample of muons (left) and protons (right).

120 Basically, different detectors only require their own geometry definitions (in gdml format)
 121 and a small number of specific detector settings.

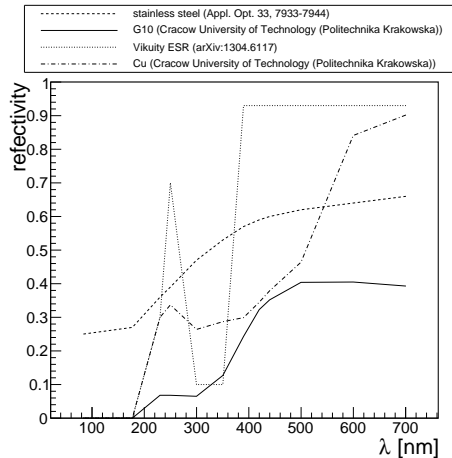


Figure 5: Reflectivity of the different materials used in the simulations.

122 The simulation of the optical photons (production and propagation) in LArSoft incor-
 123 porates two methods [12]. The **full optical simulation** implements the production and
 124 tracking of individual scintillation photons using Geant4. To produce a realistic detector
 125 response to the generated light, Rayleigh scattering, reflections, wavelength shifting and
 126 absorption are considered in the tracking of light. The relevant reflectivities included in the
 127 simulations, as a function of the photon wavelengths, are shown in Figure 5. The huge
 128 number of photons typically produced in a neutrino physics event makes these simulations
 129 extremely slow and CPU consuming, taking on the order of hours or even days per event.
 130 An alternative **fast optical simulation** mode has been developed to overcome this prob-
 131 lem for regular simulation tasks. This approach is based in the existence of a previously
 132 full-mode-built library of stored visibility data (visibility \equiv ratio between the number of
 133 produced and detected photons) to sample an expected detector response given an isotropic
 134 emission of light at some point in the active volume. Thus, for each energy deposition at
 135 each step, instead of generating Geant4 trackable optical photons, the fast scintillation mode
 136 predicts a certain number of these photons arriving to each optical sensitive volume. With
 137 this procedure, the simulation of an event typically takes minutes rather than hours to finish.

138 3.1 Optical library generation

139 For the generation of the library required by the fast optical simulation, we divided the
 140 active volume of our detector into 3D pixels or voxels (*voxelization*). To have voxels with
 141 5 cm in each dimension ($x = 200$ cm drift, $y = 400$ cm height and $z = 500$ cm length) we
 142 defined 40, 80 and 100 voxels in the x , y and z directions. Subsequently, 400k photons were
 143 randomly generated in each of these regions. This was done by a module in LArSoft that
 144 generates a source of isotropically produced Geant4 photons from any specified area in the
 145 detector. This light was simulated following a gaussian energy spectrum centered at 9.69 eV

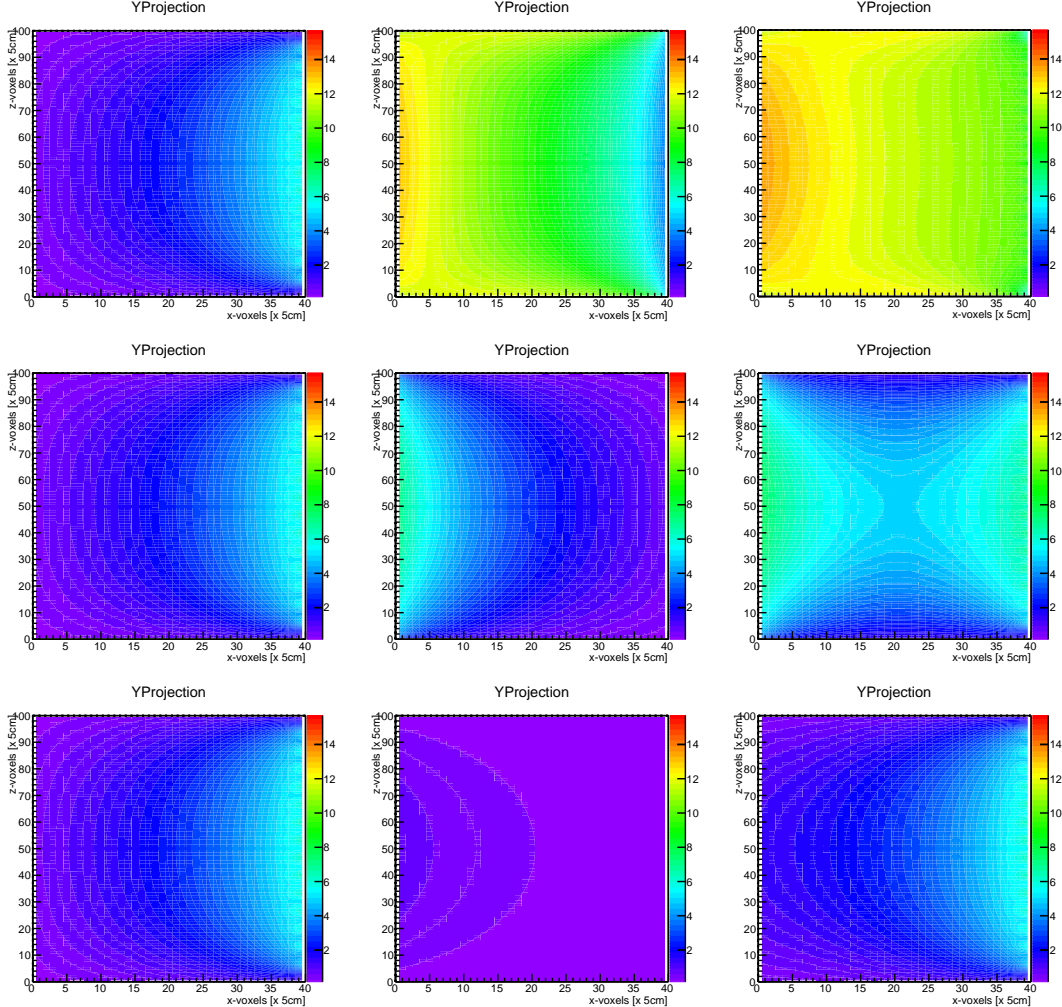


Figure 6: Visibility summed for every optical detector projected down the Y dimension (i.e., the total visibility summed for every Y at each XZ point). The visibility maps have been built using the three libraries generated for SBND (see text for details). Top is the “full coverage” configuration, middle is the “cathode only” configuration and bottom is a transparent cathode with no foils.

146 and with a width of 0.25 eV to imitate the scintillation emission in liquid argon [13]. This
 147 resulted in an extremely large (1.28×10^{11}) number of photons to be tracked, with Rayleigh
 148 scattering, reflections, absorptions and wavelength shiftings, consuming significant amounts
 149 of CPU time and memory.

150 One way of testing the system is by using *visibility maps* across the detector. Figure 6
 151 shows different examples. The YProjection histograms show the visibility summed for every
 152 optical detector projected down y (height) direction. In other words, the YProjection rep-
 153 presents the total probability of a photon to reach a PMT summed for every y at each (x, z)
 154 position. Thus, they are representations of the photon detection efficiency of our detector.
 155 In Figure 6, the top panels represent the VUV (left), visible (center) and total (right) light
 156 components for the “full coverage” configuration. The same is shown by the central panels
 157 but in this case for the “cathode only” configuration. The visibility maps in the bottom have
 158 been built using the library with a transparent cathode, representing the VUV component
 159 in the TPC where the scintillation is happening (left), the VUV component in the TPC after
 160 the cathode (center), and the sum of both components (right). The main result derived from
 161 these figures is that a PMT-based LDS including reflector foils provides a more efficient and
 162 uniform collection of the scintillation light along the whole detector volume.

163 *3.2 Arrival time distributions*

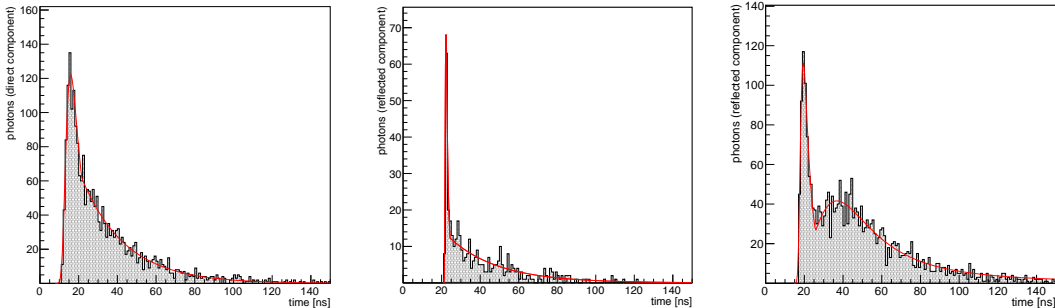


Figure 7: Examples of the arrival time distributions recorded by one PMT for the direct (left) and the reflected light components, for a detector with TPB-coated reflector foils covering the cathode (center) and the whole active volume (right). The red lines represent the fits of the distributions to the models used to obtain the parametrization.

164 The scintillation light emission in LAr is governed by its double exponential decay form
 165 (fast and slow components) and is independent of the position of the event in the detector.
 166 The second order effects due to direct transport and Rayleigh scattering were not available
 167 from the optical library method, which did not store any timing information for the de-
 168 tected photons. These effects are enhanced as the path traveled by the photons until being
 169 detected increases. Since reproducing the arrival times of these photons would require stor-
 170 ing distributions and not single numbers, their inclusion into the library would explode the
 171 memory usage of the simulation. As an alternative, we adopted the strategy of attempting
 172 to parametrize the timing distribution due to propagation as a function of the position of
 173 the light emission. We found that this is indeed possible using only the arrival time of the
 174 first photon, given by the locations of the PMT and the scintillation point. Therefore, no
 175 extra information was needed in the optical library. This works quite well for the case of the
 176 direct, VUV, light. For the reflected, visible, light the first photon arrival times were taken
 177 directly from the Monte Carlo during library generation rather than through an analytical
 178 calculation (as was done for the direct VUV light). This was saved as an additional number
 179 in the library for each voxel without noticeable impact on the memory.

180 Figure 7 (left) shows a typical photon arrival time distribution for the direct light com-
 181 ponent. A prompt signal followed by a diffuse tail are clearly detectable. To model the
 182 shape of these distributions, we have used a landau plus an exponential function (red curve
 183 on the figure). An example of the time distribution for the reflected light component in a

184 detector with reflector foils covering the cathode (center) and the full active volume (right)
185 as described in section 2, are also shown in Fig. 7. In these cases, again a landau plus an
186 exponential and a sum of two landau functions respectively have been the models adopted
187 to describe their shapes. For a LDS without these foils, the reflected component would be
188 shaped and reduced by about 80 – 90% (depending on the distance to the photocathode),
189 being the VUV light essentially absorbed by the field cage, made from FR4 printed circuit
190 panels with parallel copper strips, surrounding the LAr active volume.

191 Once we identified the models to describe the arrival time distribution of the scintillation
192 photons due to propagation, the next step was to parametrize the parameters of the selected
193 functions with the minimum arrival time of a photon in each case^a. For this purpose, a
194 dedicated library was created. For each of the different geometry configurations, 3×10^6
195 optical photons were generated and Geant4 tracked (using the full optical mode in LArSoft)
196 in 800 different positions uniformly distributed in the liquid argon active volume. With the
197 aim of obtaining the parameters describing the different light signals, we made a fit with
198 the functions described above of the photon arrival time distributions in each PMT for all
199 the sampled locations in the detector. Figures 24, 25, 28 and 29 show the results of these
200 parametrizations for the case of the direct light and the reflected light for the “cathode only”
201 and “full coverage” configurations respectively. This shows that we are able to reproduce
202 the distribution of photon arrival times for all voxels - PMT pairs in all three configurations.
203 For a full description of the different parametrizations go to Appendix A.

204 4 Timing resolution

205 The information carried by scintillation light arrives orders of magnitude more quickly than
206 that from the drifting charge. This allows its use for establishing the interaction time, t_0 ,
207 of all events. For signal events this can be used to select frames with an interaction in
208 coincidence with the beam window, allowing discarding readout frames with no neutrino
209 interaction. In parallel it can be used to tag out of beam events both background like cosmic
210 rays and their daughters or signals like supernova neutrinos or other exotics. Knowing the t_0
211 is needed to translate the drift time of the ionization electrons into the x-position in the TPC
212 where they originated. Given the relatively slow drift speeds of the electrons this translation
213 does not require timing resolution better than several hundreds of nanoseconds (of the order
214 of one time-tick of the charge ADC). Improving the timing resolution, combined with good
215 positional resolution could improve background reduction, e.g. resolving the beam timing
216 buckets or identifying the start or end of a muon track. It could even open new possibilities
217 in terms of physics capabilities, e.g. by identifying Kaon decay timing structure or even
218 by tagging heavy dark matter particles arriving later than the beam buckets. These would
219 require the timing resolution to be of the order of nanoseconds.

220 The SBND LDS electronics will most likely have the capability to resolve timing of the
221 order of nanoseconds and so one of the objectives of the simulation work was to determine
222 whether such resolution in a large liquid argon detector is even possible. The resolution will
223 be affected by the spread of velocities and the steep refractive index at VUV wavelengths and
224 the potential smearing of the photon group velocities as well as distortions due to transport
225 effects like Rayleigh scattering. Because the group velocity of the visible component is
226 significantly higher than that of the VUV component, see Fig. 1, there was a suspicion that
227 the timing resolution of the whole system could be affected by the visible light washing out
228 the VUV component.

229 To test the intrinsic timing resolution of the detector we used point-like sources and
230 diffuse proton tracks, described in Sec. 2. We looked at the spread of the first photon arrival
231 times to give us an idea of the expected jitter of their arrival times. We then translated
232 that into a rough, intrinsic timing resolution of the detector using a correction based on the
233 distance of the event from the PMTs (obtainable from the charge information). Finally, we
234 report on the effect that the transport of the photons in liquid argon has on the effective
235 decay times of the liquid argon scintillation components.

^aFor the direct light component this is calculated simply by the ratio between the voxel-PMT distance and the group velocity of the VUV photons generated in the liquid argon scintillation.

236 *4.1 Spread of first-photon arrival times*

237 In order to understand the effects of Rayleigh scattering and emission width of the VUV light
238 on the expected jitter of the first arriving photons, we looked for different energy events, both
239 point-like and diffuse. The expectation was that for lower energy events the smaller number
240 of photons arriving at the PMTs would lead to a larger jitter and therefore worse timing
241 resolution than for higher energy events where the large number of photons would ensure
242 that at least some of the “fastest” photons would be detected.

243 For each energy we looked at the arrival times of the first photons compared to the
244 minimum expected photon flight time in different energy bins. An example bin is shown in
245 Fig. 8 top-left, with the blue points corresponding to VUV, direct photons and the red to
246 Visible, reflected ones. For the VUV light the minimum flight time is directly translateable
247 to the distance via $t = x/c_{VUV}$. For the visible light it is a parameter calculated during
248 the simulation (and saved into the optical library) which is effectively the shortest path the
249 reflected light need travel to reach a PMT. For each set of x, y, z coordinates and PMT
250 position this is a precisely defined number. The plots are presented in this manner to show
251 where the Visible light actually may have a chance to arrive before the VUV light. Note that
252 for the case of the visible light, this time becomes smaller the closer we are to the cathode
253 (the opposite of direct light), as these photons have to travel from the scintillation point
254 to the cathode, and after reflected (reemitted) by the TPB-foils they have to travel to the
255 photocathode plane.

256 The first noteable thing is the increase of the spread of arrival times with the growing
257 minimum arrival time. This can be intuitively understood, given that the longer the light
258 travels the more opportunities the transport has to affect the arrival times. This effect is
259 quantified in the remaining plots in Fig. 8, where each point essentially corresponds to the
260 RMS in one of the single energy plots shown in the top left. In both detector configurations
261 using the reflective foils the visible light arrives at earliest around 12ns after the energy
262 deposition, for events extremely close to the cathode. The spread of this light ~ 0.3 ns is
263 much smaller than that of the VUV light coming from that far ~ 2 ns, suggesting that the
264 reflected light might actually improve the timing resolution of events close to the cathode
265 planes. In the case of the transparent cathode, Fig. 8, bottom-right, shows that the jitter of
266 the arrival time of the first photons becomes of the order of ~ 10 ns for photons arriving at
267 PMTs in the adjacent TPC.

268 *4.2 Distance corrected timing resolution*

269 In order to determine the timing resolution of the total detector system, the registered arrival
270 time needs to be compared to the original time of the event deposition. This leads to a small
271 bootstrapping problem, as this time is normally obtained using the scintillation light itself.
272 This problem can be resolved thanks to the excellent positional resolution of the TPC. Using
273 an iterative approach allows to first determine the x-position of an event using even a very
274 rough determination of t_0 utilizing the scintillation light pulse. Then, having calculated the
275 x-position of a track, one can calculate the expected arrival time of both VUV and Visible
276 photons using the method shown in Fig. 9. This simple method assumes a one-dimensional
277 path along the x-direction of the photon either directly to the PMT (VUV light) or to
278 the cathode and then back to the PMT (Visible light). It is possible to imaging a more
279 precise correction method, calculated on a PMT by PMT basis, however already this simple
280 approximation is instructive.

281 The timing resolutions calculated using the iterative correction are shown in Fig. 10. The
282 corrected arrival time distributions for proton tracks of all energies shot through the TPC
283 at different drift positions were used, as described in sec. 2. Only the iterative correction
284 is applied and the x-position used is the middle of the proton track. In the plot on the left
285 both the VUV and Visible component distributions, for the “cathode only” configuration, are
286 shown separately, showing that the two distributions have similar RMS: ~ 2 ns and ~ 1.5 ns,
287 respectively. What will be observed in the detector will be actually the first arriving photon
288 and that is shown with the black distribution which seems to take the best of both worlds
289 leading to a possible resolution of ~ 1.5 ns. In the case of a transparent cathode, as expected,

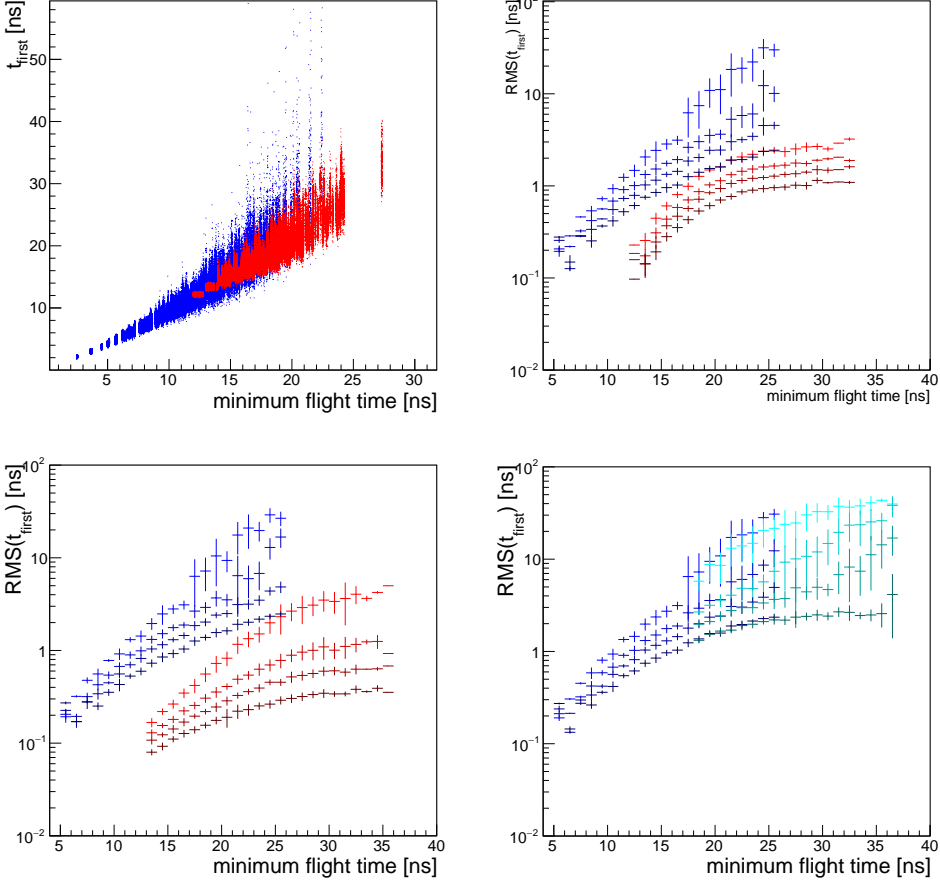


Figure 8: Reconstructed “PMT time resolution” for point-like sources and the different light components, VUV (blue), visible (red) and VUV in the second TPC (cyan), in the configurations under study. The profiles represent the spread (RMS) of the first arrival time (t_{first}) in the PMTs, as a function of the minimum time of flight, given a scintillation point for the “full coverage” (top-right), “cathode only” (bottom-left), and “transparent cathode” (bottom-right) geometries. Note that for the VUV light this translates as direct distance from energy deposition, which is not the case for the visible component where the time corresponds to the shortest path of the reflected light to the PMT. The four profiles have been calculated for 25, 75, 200 and 1000 MeV energy deposited in the liquid argon, improving the resolution with the energy (from lighter to darker), as expected. The top-left figure shows, as an example, the points used to obtain the profile for the case of 25 MeV in the ”full coverage” configuration.

290 the timing resolution of the light travelling to the other TPC through the cathode is somewhat
 291 worse, ~ 4 ns, however this component is not likely to be important for timing resolution. A
 292 small bias is present in all cases, but we expect it should be possible to map it and correct
 293 for it with a more precise analysis. See Appendix B for a description of the time resolutions
 294 before and after the bias correction described in Fig. 9, and for all the different topologies
 295 (distances to the photocathode) used separately.

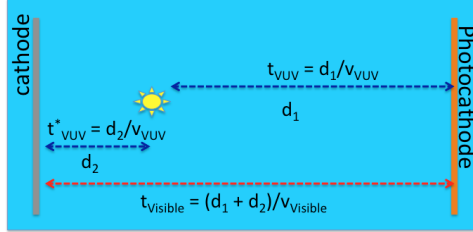


Figure 9: Schematic view of the geometrical correction applied to the first arrival times detected by the LDS in the “cathode only” configuration. A similar correction is applied to the times measured in the “70% transparent cathode” configuration (to go from Figure 32 to 33).

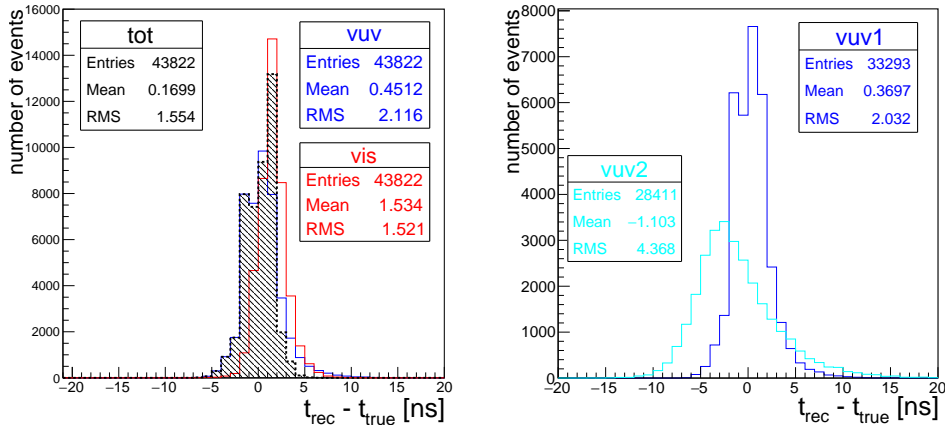


Figure 10: Expected timing resolution of an event for the VUV and Visible components in case of an opaque cathode covered by TPB-coated reflector foils (left), and a 70% transparent cathode (right). For this study we have simulated protons with energies between 20 and 500 MeV and at six different positions in the detector (see text for more details). The different colors represent the different light components detected in each configuration: VUV (blue), visible (red), total (black) and VUV in the TPC after the transparent cathode (cyan).

296 4.3 The transport effects on the values of the effective time constants

297 An important effect of the complex structure of the photon arrival times due to transport
 298 effects has been observed in the effective timing structure of the scintillation light. Through
 299 the convolution of the pure argon scintillation decay times ($\tau_{fast} = 6$ ns and $\tau_{slow} = 1590$ ns)
 300 with the effects of propagation, mainly due to Rayleigh scattering and the spread in start
 301 velocities amplified by distance traveled, the observed timing structure of argon pulses be-
 302 comes modified. When plotting an average waveform of scintillation light, as observed in
 303 Fig. 11 (left) and trying to recover the decay-time components we note that the exponential
 304 times differ significantly from the original argon values. This difference is most prominent in
 305 the short component and grows with distance from PMT as seen in Fig. 11 (right) becoming
 306 as large as 50 ns for VUV light close to the cathode. At first order this could signify that
 307 trigger methods wanting to focus on only the fast component of the scintillation light may
 308 need to correct for this effect and be forced to open a trigger window as large as ~ 150 ns
 309 instead of ~ 25 ns. This effect is opposite for the visible light which, if using a combination of

310 the two, could allow restricting ourselves to a τ_{fast} of at most 30 ns. Note that this analysis
 311 does not include the effects of the timing structure of the TPB reemission, as described in
 312 [1] resulting in a similar effect. We expect these effects to add together and result in an even
 313 more complicated and longer time structure of the fast component.

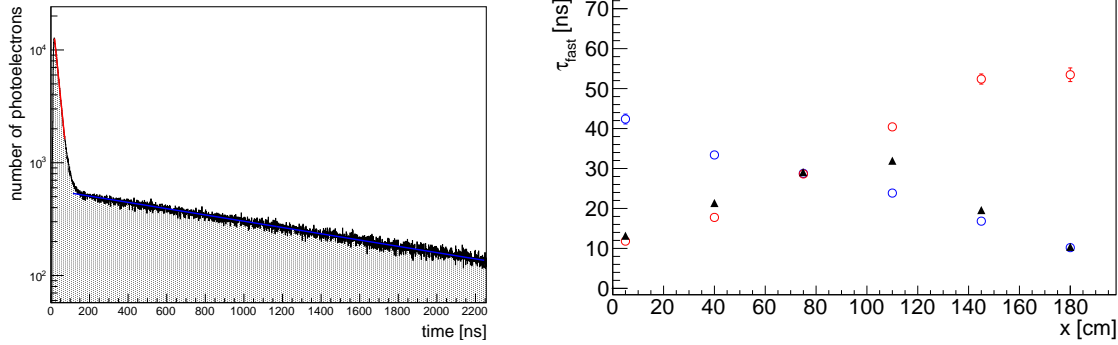


Figure 11: Left: Average VUV signal, detected by a PMT, coming from energy deposited at 100 cm from the PMTs. The decay time of the fast component is longer than expected for argon emission times caused by the convolution of the argon scintillation ($\tau_{fast} = 6$ ns and $\tau_{slow} = 1590$ ns in our simulations) and propagation (direct transport and Rayleigh scattering) times. Right: The resulting effective decay times of the fast light component reaching the PMTs have a new time structure. This modifies the original *pure scintillation* time structure of the signals, especially the fast component, in the way shown in the figure on the right, as a function of the distance to the PMT (note that $x = 0$ is the position of the cathode). For this study we have used the configuration with an opaque cathode covered by TPB-coated reflector foils: VUV (blue), visible (red) and total (black).

314 5 Calorimetric resolution

315 The amount of scintillation light emitted in liquid argon is proportional to the deposited
 316 energy making it suitable for use in calorimetric reconstruction. This has been successfully
 317 demonstrated by Dark Matter experiments, e.g. [2, 3]. To reconstruct the deposited energy
 318 with reasonable precision we either need the detector to have a relatively uniform response
 319 or we need very good mapping of the Light Yield in terms of detector coordinates and
 320 precise position reconstruction, e.g. using the TPC information in a way similar to the
 321 timing. Only in the former case would the calorimetric information be easily applicable to
 322 e.g. trigger considerations.

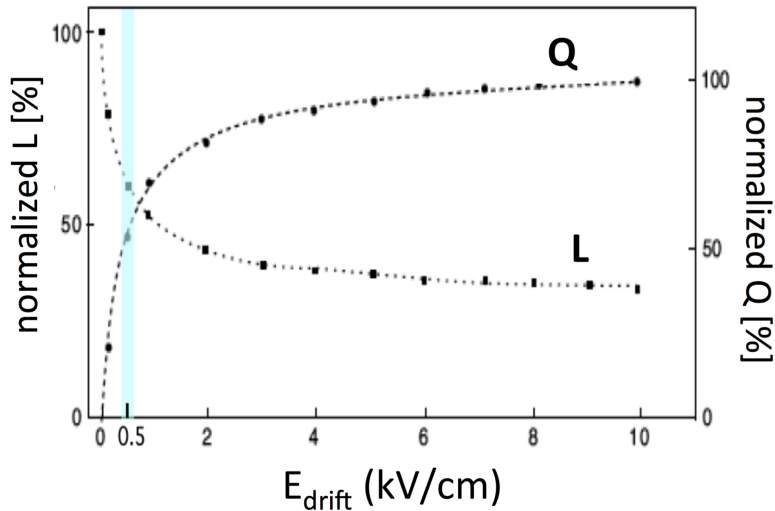


Figure 12: The fraction of light and charge emitted per energy deposition in liquid argon.

323 It has been established that in liquid argon the fraction of energy going into charge and
324 scintillation light depends on the value of the electric field, see fig. 12. It has also been
325 demonstrated that due to recombination and quenching effects, non-linear effects appear at
326 high energy loss rates [4] requiring corrections, e.g. the Birks correction when reconstructing
327 energy using charge only. Scintillation light could be potentially used to help with those
328 corrections or be used as a standalone energy reconstruction method, especially for low
329 energy events.

330 *5.1 Light Yield*

331 To test the applicability of scintillation light to energy reconstruction in a liquid argon
332 detector at neutrino energies our first step was to determine the general efficiency of detecting
333 photons per unit of deposited energy also known as Light Yield (LY). Fig. 13 shows the
334 average number of photons detected by all of the PMTs per MeV of deposited unit energy.
335 These plots are obtained by shooting test point sources along a line going from the middle
336 of the cathode plane to the middle of the anode plane i.e. $(y, z) = (0, 250)$ cm. The three
337 setups shown are: the transparent cathode (top left, cyan representing light exiting to the
338 othe TPC area), only the cathode covered with reflector foils (top-right) and whole fieldcage
339 covered with foils (bottom). As expected, the efficiency of collecting direct VUV light (dark
340 blue) falls with the distance from the cathode. The collection efficiency changes by about
341 one order of magnitude (~ 120 phel $\rightarrow \sim 15$ phel) from the wires to the cathode plane. In
342 case the cathode is transparent very little light makes it to the other TPC compared with
343 the in-TPC light (~ 0 phel $\rightarrow \sim 12$ phel). One can note that the small amount of light seen
344 in the other TPC means that the disuniformity will be smaller in terms of absolute number
345 of phel than for the in-TPC case.

346 In both set-ups using the reflector foils, the visible component, i.e. the wavelength shifted
347 light reflected off the foils (red), exhibits a behaviour opposite to the VUV light. The highest
348 collection efficiency occurs for energy deposited close to the CPA plane and falls the closer
349 it gets to the PMTs. This effect is easy to understand through geometric considerations.
350 The result is that summing the two components together (black) results in a very uniform
351 light collection efficiency along the drift length. In the full coverage set-up the resulting light
352 yield is estimated to be on the order of 200 – 240 phel (full coverage) and 130 – 150 phel
353 (cathode-only coverage).

354 These plots give a general idea about the uniformity of light collection, however they
355 are based on the idealised case of points located in the middle of the cathode plane. To
356 understand the uniformity throughout the whole detector we added points close to the field-
357 cage walls (25 cm from the side and top walls) and compared their behaviour to those along
358 the center of the detector. Considering these two extreme cases, shown in Fig. 14 gives a
359 better estimate of the total uniformity of the detector response in scintillation light. In the
360 case of full foil coverage the total response (black band) is extremely uniform despite the
361 fluctuations in the composite VUV and visible components. In the case of the cathode-only
362 setup the total uniformity is not as good, however still allows setting an energy threshold
363 indepent of x location in the detector.

364 *5.2 Reconstructing Missing Hadronic Energy*

365 A possible application of a high LY LDS in a neutrino detector is the reconstruction of missing
366 hadronic energy. When using the TPC to resonctruct the original energy of particles, e.g.
367 protons, we can base ourselves on the distance the particle travels and compare it with
368 NIST tables which correlate distance traveled with kinetic energy. This method has been
369 demonstrated to work by the ArgoNeuT experiment, [4]. Fig. 15 shows our reproduction
370 of that result in our simulation. The caveat is that for this method to work the proton
371 cannot lose too much energy inelastically. Even for these events the effective track lengths
372 are shorter than expected and the deposited energy is lower than the total. This can be
373 recovered to some extent by using scintillation light methods, which correspond to the white
374 points, which are closer to the dashed line signifying the NIST expectations.

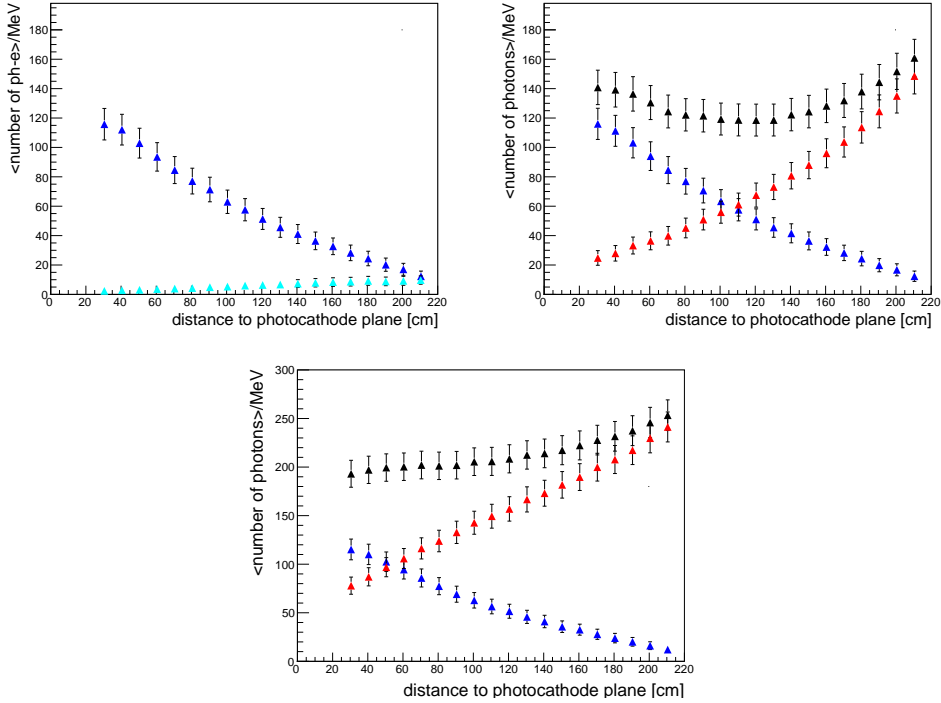


Figure 13: Average number of detected photons per MeV as a function of the distance to the photocathode plane for a geometry with i) a 70% transparent cathode (up-left), ii) an opaque cathode covered by TPB-coated reflector foils (top-right), and iii) TPB-coated reflector foils covering the active volume of the TPC (bottom). To compute these light yields, we have generated the scintillation photons in points at the center of the photocathode plane (0, 250) cm at different drift distances, assuming a PMT quantum efficiency of 20% and a scintillation yield of $19200 \gamma/\text{MeV}$. The different colors represent the different light components detected in each configuration: VUV (blue), visible (red), total (black) and VUV in the TPC after the transparent cathode (cyan).

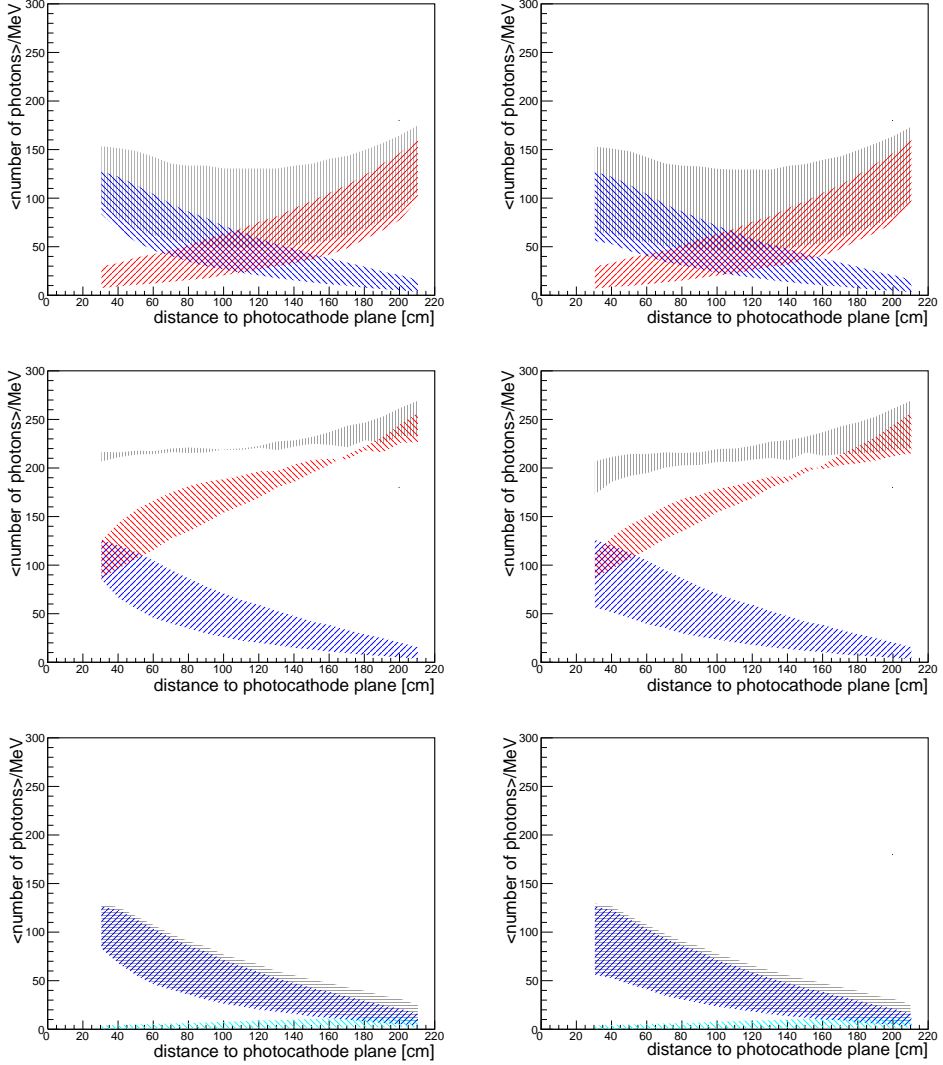


Figure 14: Light yield value regions for the "cathode only" (top), the "full coverage" (middle) and transparent cathode (bottom) configurations. Figure 13 represents the maximum values in each of these regions, as the scintillation points are centered in the photocathode plane, maximizing the light collection efficiency. But when we move along the TPC, due to the nonuniformity of the LDS, we measure different (smaller as we move away of the photocathode plane center) light yields. In each plot, the regions are defined by scintillation points generated at the center of the photocathode plane (maximum), and at 25 cm away from the y/height (left) and the z/length (right) edges of that plane (minimum).

According to the MC for about 10% of protons a large fraction of the energy is carried away by neutrons which themselves are invisible to the TPC. The neutrons recoil often inside the TPC resulting in charged particles that produce ionization electrons which will arrive at the anode planes, see e.g. Fig. 16. The amounts of charge from these recoils, are relatively small though, and therefore difficult to detect via the TPC. The scintillation light on the other hand might be of use, any light emitted by the neutron recoils will be automatically summed up in the PMTs possibly resulting in a better reconstruction of the total deposited energy. This is represented in fig. 17, where we compare the precision of using the track length and scintillation light as a measurer of the proton energy. We observe that the scintillation light provides a better observable to reconstruct the energy deposited by protons, even in cases where they interact non-elastically.

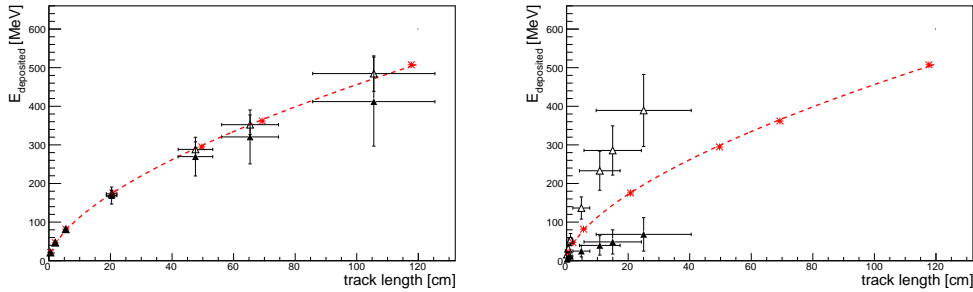


Figure 15: The correlation of proton track length with the deposited energy by the proton for tracks with > 70% of energy belonging to the proton track (left, “well behaved proton tracks”) and for events where a significant part of the energy was carried away by inelastic interactions (right, “not well behaved proton tracks”) - black full points. The dashed line shows the NIST measured correlation of proton kinetic energy and track length and the red points show the position of the proton events used based on their original kinetic energy. The white points correspond to the total deposited energy, presumably recoverable through scintillation light.

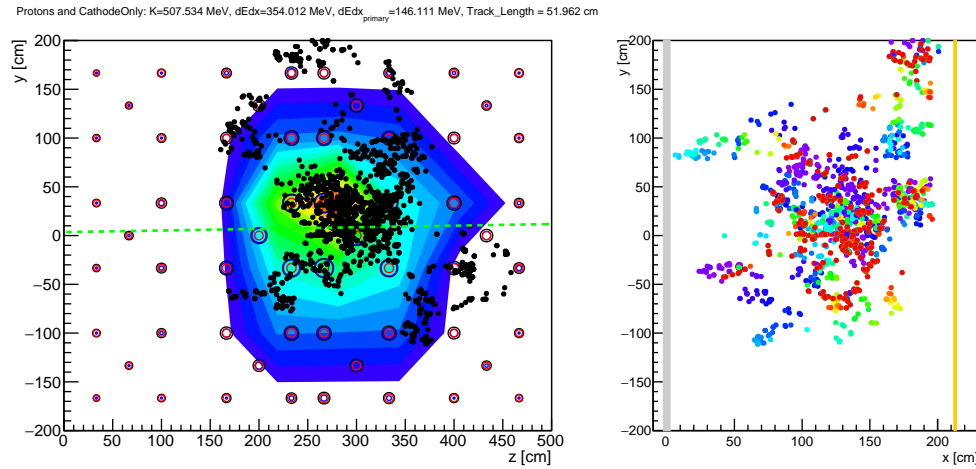


Figure 16: Example of proton event with a quick inelastic interaction. There is no recoverable track (or very underestimated), and so the energy reconstruction would have to be based on using scintillation light.

5.3 Energy Resolution

The final parameter to test is the anticipated precision of determining the deposited energy of a single, well behaved track. The results of this study are shown in Fig. 18, where on the plots on the left we see the difference in ideal energy resolution for proton tracks in an energy range from 20 to 500 MeV kinetic energy and moving parallel to the photocathode plane. As expected the resolution becomes better with higher energy of the track, because of

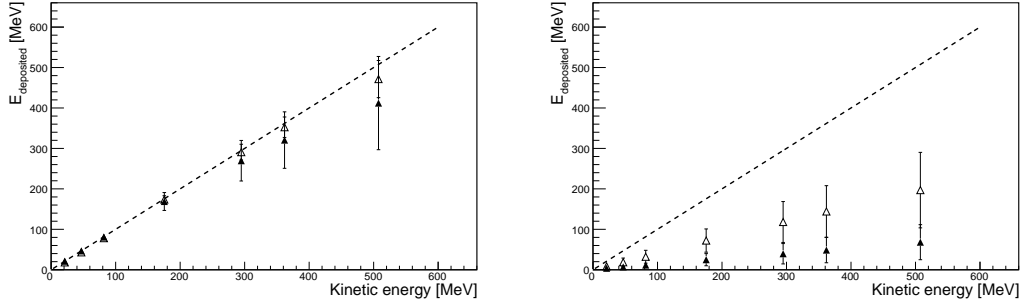


Figure 17: The efficient of reconstructing the proton energy using the NIST track length method for proton tracks with $> 70\%$ of energy belonging to the proton track (left, “well behaved proton tracks”) and for events where a significant part of the energy was carried away by inelastic interactions (right, “not well behaved proton tracks”) - black full points. The dashed line shows perfect 1:1 reconstruction. The white points correspond to the total deposited energy, presumably recoverable through scintillation light.

the statistics of the arriving photons become larger. The in-TPC resolution is significantly better than the out-of-TPC resolution for the same reason. A very interesting effect was observed when we remove the $x = \text{const.}$ constrain, i.e., leaving the proton path as it is, shown in Fig. 18, right. This caused the energy resolution of the proton tracks become significantly worse with growing energy. This is an effect of the highest energy tracks also being the longest and therefore traversing significant distances in the detector. Given that at different distances the light yield is different, as shown in Fig. 13, this results in different parts of the track emitting light at different efficiencies depending on their direction and not energy. This effect can be mitigated by using the total light, as shown by the black bands in Fig. 18 (right). In principle, knowing the path of the track and direction should allow to correct for this effect in case the reflective foils are not present.

Appendix C contains the plots for other positions where we looked at the proton tracks, analogous to those shown in Fig. 18.

6 Position resolution

The final important application of scintillation in a liquid argon neutrino detector is the determination of the position of the events that generate the light flashes. The positional resolution using the scintillation light system will never be as good as that obtained using the TPC information (which needs the t_0 from scintillation light). Even so, a rudimentary position resolution with light is extremely important as it will help resolve the degeneracies between multiple tracks inside one event frame. In a surface TPC like SBND this is crucial to identify which event happened inside of the beamgate (signal) and which happened outside of it (background). The loss of positional resolution as a result of adding new components, e.g. reflective foils, would be a strong argument against such an addition.

In previous detectors using scintillation light, e.g. MicroBooNE [10] positional reconstruction was attempted only in the coordinates spanning the anode/cathode planes, i.e. the y - z plane. The positional reconstruction then depends on the spacing between different PMTs and the relative differences between the charge registered by each PMT. Reconstruction in the x -position is impossible using scintillation light, unless we have a way to measure a difference in arrival times of the arriving light in both directions. Knowledge of the path the light took to arrive at PMTs leads to translating the difference into a position in the x -component.

6.1 y - z (anode plane) resolution

Given the large number of optical channels that SBND will have at its disposal we can expect that the y - z position resolution should be significantly better than e.g. predicted for MicroBooNE. In this work we present results using a calculation of the baricenter, i.e.

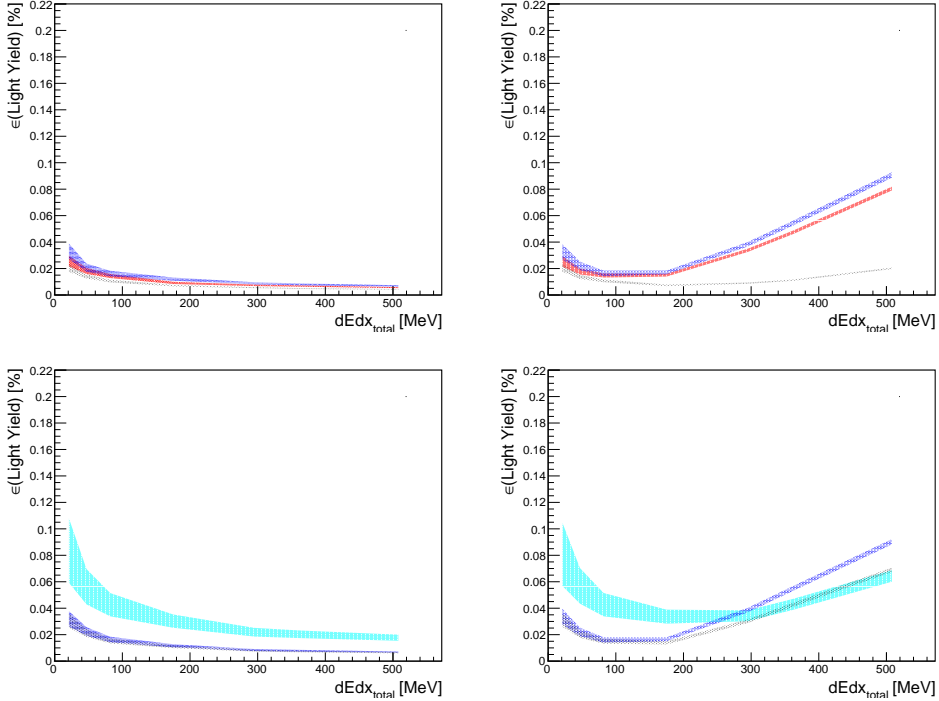


Figure 18: Relative uncertainty of the detected light yield as a function of the energy deposited in the LAr active volume for a sample of protons injected close to the center of the TPC (85 cm, 0, 250 cm) in the beam direction. The geometry used in the top plots was the “cathode only” configuration, where you can see the results for the total (black), VUV (blue) and visible (red) components. A geometry with a 70% transparent cathode was used in the bottom plots, with the VUV light detected in the TPC where the protons were injected (blue), and in the second TPC after the cathode (cyan). The difference between the left and the right plots is that in the former, we have imposed to the proton traces to be parallel to the photocathode plane ($x = \text{const.}$ in all steps), while in the plots on the right, the traces were simulated in the $\theta \pm 10^\circ$ and $\phi \pm 10^\circ$ angular window. The deviation from the expected behaviour (illustrated in the left panels) is due to the nonuniformity of the light yield along the detector (Figures 13 and 14).

427 the charge weighted mean of the (y , z) coordinates of the PMTs that see scintillation light
 428 signals. The results of this calculation are compared against the y and z coordinates of the
 429 particles that generate them in Fig. 19. The top two plots show the resolution for point-
 430 like energy depositions, where we used proton tracks with kinetic energies < 200 MeV. The
 431 obtained resolution is excellent both in the y and z position suggesting the possibility of
 432 a better than 10 cm resolution in the detector. Applying this algorithm for more diffuse
 433 tracks yields slightly worse results, as the uncertainty due to the LDS is combined with the
 434 uncertainty stemming from the non-negligible path of the particle in the detector (we use the
 435 averaged mean of the track as the values of y_{true} and z_{true}). In this case the resolution using
 436 the visible component is somewhat worse than that from the VUV. The resolution of the
 437 total arriving light is however still of the order of ~ 20 cm in both directions, which is a
 438 significant improvement with what is expected by MicroBooNE. It is expected that using a
 439 more sophisticated algorithm, e.g. a likelihood fitter, would improve the positional resolution
 440 for diffuse tracks.

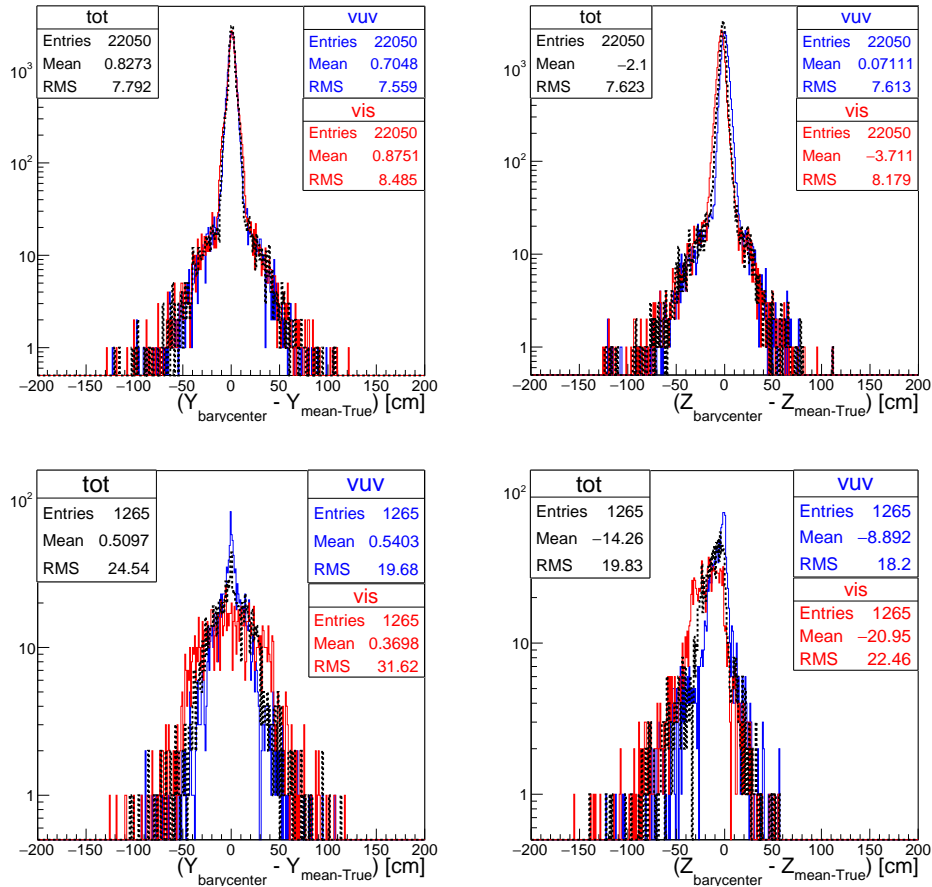


Figure 19: Estimation of the “mean position”, in the photocathode plane (z , y), for a sample of protons generated randomly ($\Delta\theta = \pm 180^\circ$, $\Delta\phi = \pm 180^\circ$) in the center of the TPC (100, 0, 250) cm. The different colors represent the results for the different light components for a geometry with an opaque cathode covered by TPB-coated reflector foils: total (black), VUV (blue) and visible (red). The top panels show the results for point-like protons ($E \leq 200$ MeV), while in the bottom panels the energy of the protons is ~ 500 MeV (“extended tracks”).

We have also investigated the possibilities of using the scintillation light to reconstruct start and end points of tracks. Fig. 20 shows an example of an event display with a contour drawn based on the fraction of light seen by separate PMTs. This contour, as well as those shown in figs: 40, 41, 42, 43 and 44 found in Appendix D show that a simple algorithm selecting PMTs with a fraction of light - in this case 50% - does an excellent job in localizing the area in which the track interacted. Using the charge amounts deposited in the contour

PMTs allows fitting a straight line (dashed green in Fig. 20) which in most cases reproduces the original charge track reasonably well. Combining the information from the track direction hypothesis and the light contour allows computing an estimate of the track start and end points. The results of this estimation are shown in Fig. 20), right, where we can see that a resolution of ~ 40 cm seems plausible even given this crude algorithm. This gives reasonable hope that with more efficient algorithms we could tag entering cosmic/dirt events using scintillation light which could significantly improve our trigger purity.

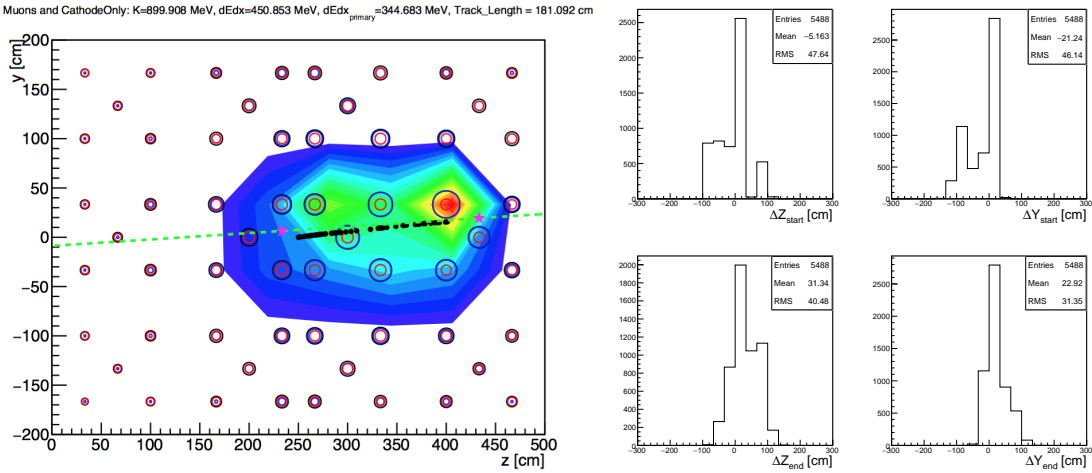


Figure 20: Left: Footprint of the light signals in the photocathode plane generated by a *cosmic* (~ 1 GeV muon) in a geometry with an opaque cathode covered by TPB-coated reflector foils. Each circle represents the position of one PMT, and the size of the circles are proportional to the log of the signals: total (black), VUV (blue) and visible (red). The contour has been defined by the “hottest” PMTs containing the 50% of the total light. For a rough estimation of the direction of the track, a linear fit to the contour is done (dashed green line). By comparing the edges of the contour with the fit we compute the *start/end* points of the *cosmic* (pink stars in the figure). Right: Resolution in the estimation of the (z , y) *start* (top) and *end* (bottom) points for a sample of *cosmics* (~ 1 GeV muons) with different topologies (see text for details). The results when using the VUV or the visible components are very similar (see Appendix C).

454 6.2 x (drift) resolution

A new possibility open to SBND that was not feasible in previous detectors is the reconstruction of the x -position using scintillation light only. This generally requires measuring a difference in arrival times of the light going out in both directions from the interaction point. This can be achieved either through a transparent cathode where PMTs at the ends of both TPCs can see the light from an event and the difference between the two arrival times can be translated into the x -coordinate of the original event. An alternative method is to use an optical-TPC like method where if light reflected off of an opaque cathode is registered with the same PMTs and the difference in arrival times can be resolved this results in a reconstruction identical to the two TPC method. In liquid argon the latter method would be difficult to use without using wavelength-shifter covered reflector foils, because of the low VUV reflectance and the structure of the scintillation light which would make it more difficult to resolve the first and second peak. Installing the WLS-covered foils enables this feature, firstly by ensuring that the light is efficiently reflected off of the cathode and secondly due to the fact that it adds the new, visible, component to the scintillation light. If some PMTs are then not coated with TPB they would only be sensitive to the visible component, opening the possibility of comparing the arrival times on neighboring PMTs and using them to extract the difference in arrival times of the two components again translating it into a position in the x -coordinate. The results of these operations are shown in Fig. 21.

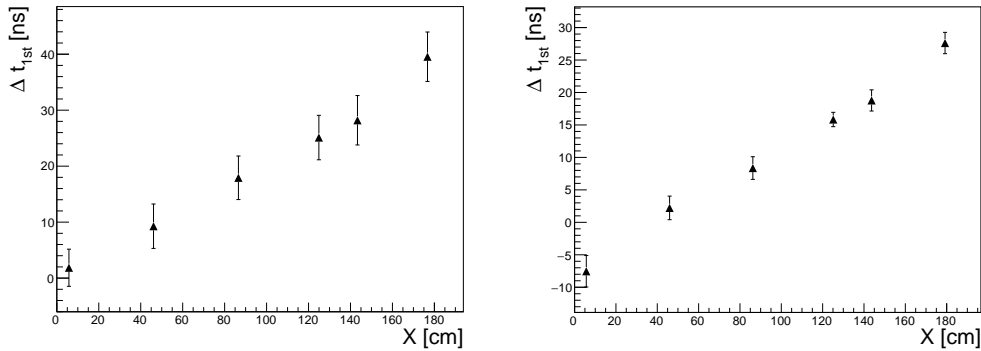


Figure 21: x-position resolution using transparent cathode (left) and using difference between visible and VUV light (right). Note that in the 2 TPC method for a class of low energy events the light will not make it to the other TPC making it impossible to use this method.

473 7 Saturation studies

474 The 8" photomultipliers to be used in SBND may suffer saturation when a signal is particu-
 475 larly large due to the small distance of the PMT with the event (scintillation region), and/or
 476 the large energy deposited in the liquid argon. The saturation condition, will be determined
 477 by the electronics configuration, in particular the sampling frequency and dynamic range
 478 of the system. Another factor is the PMT non-linear response which is expected to appear
 479 for anode peak currents above a certain value. From ICARUS R5912MOD (10 stage) PMT
 480 testing, the gain is linear up to about 400 photoelectrons.

481 In this section we study, using our simulations, the saturation probability of our PMTs
 482 as a function of the distance and the energy deposition in the detector active volume, for
 483 the three light components of the "cathode only" configuration. To do that, we assume
 484 an electronics with a sampling frequency of 500 MHz and a 14 bits dynamic range. We
 485 define the saturation condition as occurring with 500 photoelectrons. We currently ignore the
 486 nonlinearity gain effects of the PMT. The spread in time used for the single photoelectron
 487 response (SER) is shown in Figure 22^b. Our saturation condition together with our 14 bits
 488 digitizer will set the amplitude of our SER signal to a value of 32 adc counts ($2 \times 10^{14}/500 \sim 32$).
 489 With all these ingredients, and using our sample of protons, we have built the PMT
 490 saturation maps shown in Figure 23 top panels. As mentioned before, these results are very
 491 sensitive to the particular electronics we are using. As an example, if we change the SER
 492 time spread to a value of 10 ns the results change to the bottom panels on Figure 23. A
 493 remarkable result coming out from these maps is that the visible light does not contribute
 494 (or negligibly) to the saturation of the PMTs.

495 8 Conclusions

496 We have built a LArSoft based simulation package to study the behaviour of the SBND Light
 497 Detection System options under considerations. We have compared a setup looking at only
 498 direct (VUV) light and a transparent and opaque cathode with a system where either the
 499 whole field cage or the cathode only is covered with wavelength-shifting reflector foils. We
 500 have studied the performance of these different configurations in terms of timing, energy and
 501 position resolution. We also began studies of the effects of the increased light yield of these
 502 setups on the electronics and trigger considerations of the detector. We found that adding the
 503 reflector foils improves the performance of the LDS in terms of timing and energy resolution
 504 and does not degrade the positional resolution provided only the cathode is covered in foils.

^bIn practice we have used a gaussian function with $\sigma = 1.02$ ns.

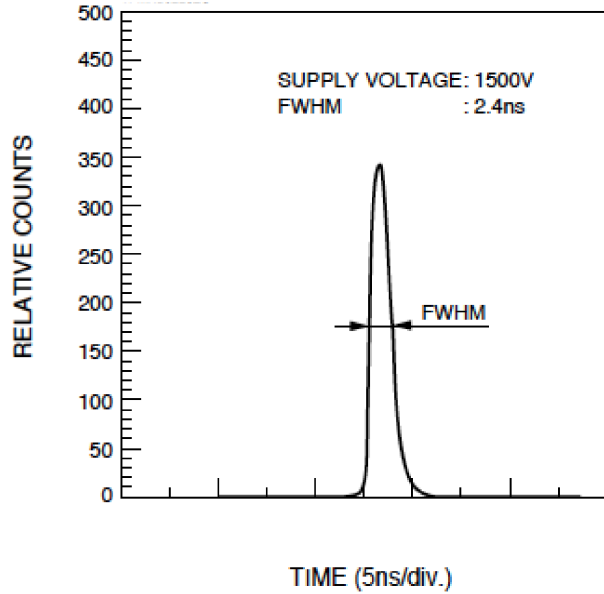


Figure 22: Single Electron Response used in this study. The amplitude in adc counts was set to the value of 32.

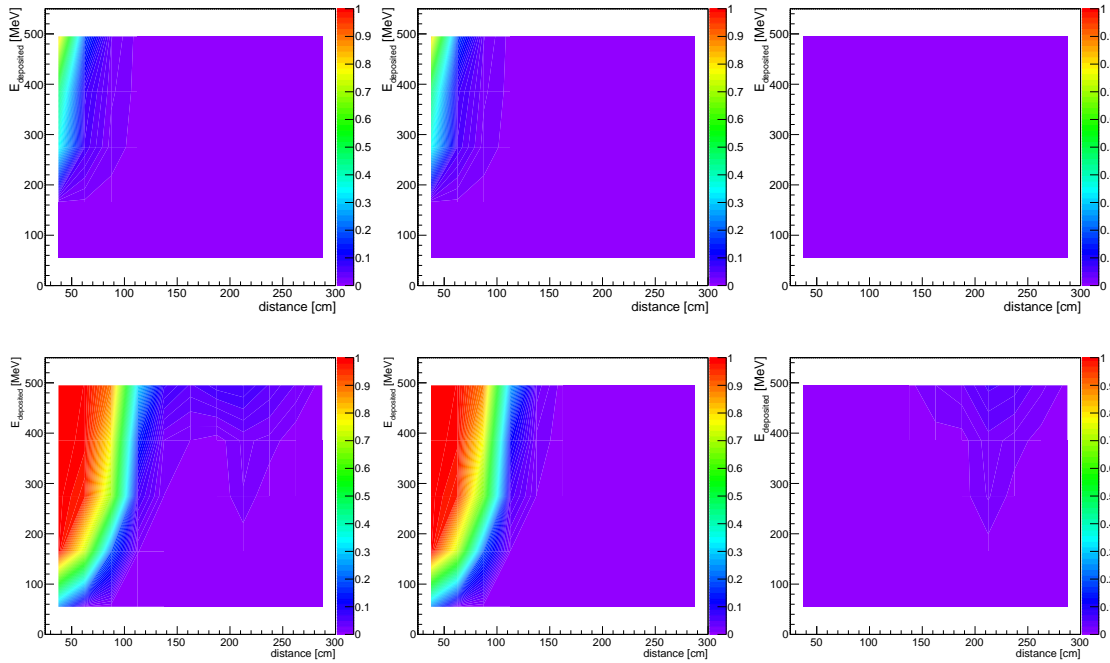
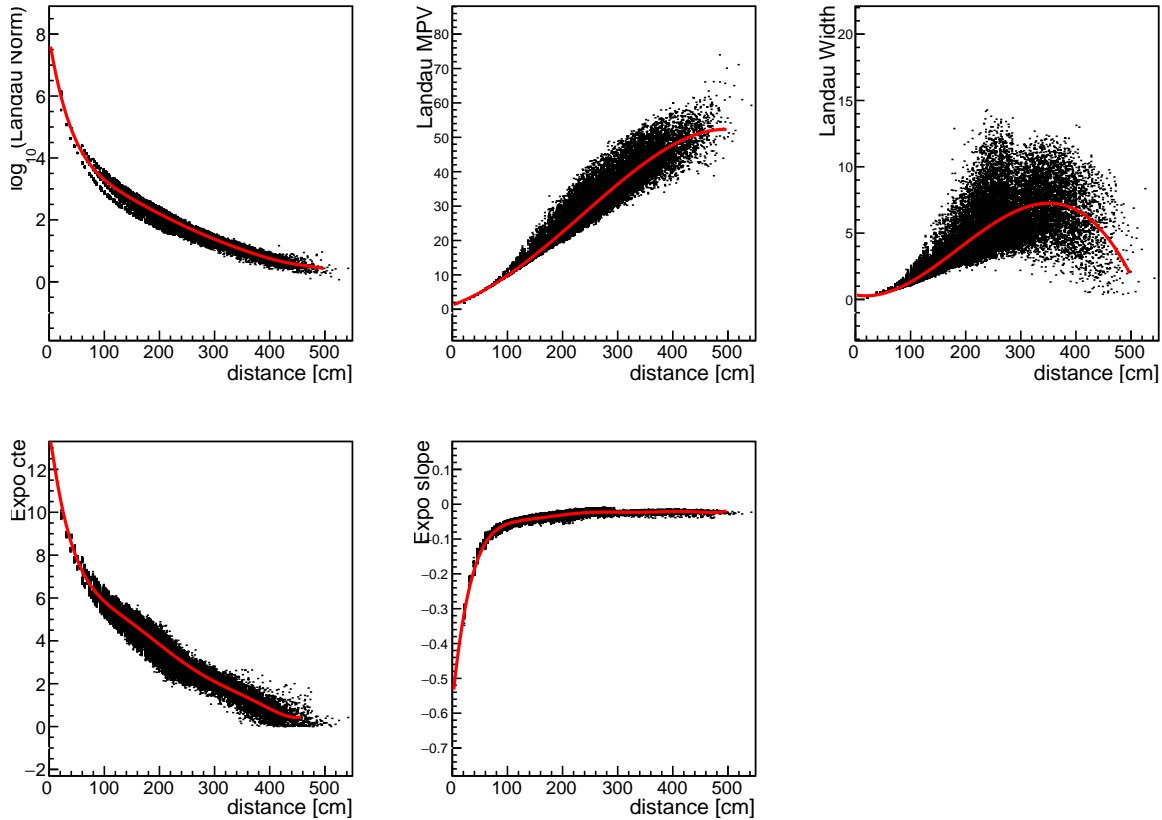


Figure 23: Saturation probability of a PMT, as a function of the distance and the energy deposited in the liquid argon, for the total (left), VUV (center) and visible (right) components. For this study we have used our sample of protons in a geometry with an opaque cathode covered by TPB-coated reflector foils. The difference between the top and bottom panels is the width of the SER signal, being ~ 1 ns and 10 ns respectively. We see how the visible light does not contribute to the saturation probability in any case.

505 A Simulation Performance Plots

506 We have modeled the arrival time of the photons in the different LDSs under study (see
 507 Fig. 7). For the case of the VUV, direct, light we have used a landau + exponential function.
 508 The five parameters of this function have been parametrized as a function of the position
 509 of the light emission. For that we used the arrival time of the first photon (t_0), given by
 510 the locations of the PMT and the scintillation point. For the case of the direct light (VUV)
 511 this is essentially equivalent to use the distance. You can see the results in Fig. 24. All the
 512 parameters describe a good correlation with the distance. Although a weaker dependence
 513 is observed in the case of the landau width. Notice that the relevant parameter for most of
 514 the timing studies would be the landau MPV where the correlation is very strong, while the
 515 time structure will be affected by all the parameters. The red line represents the polynomial
 516 fit in each case.



517 Figure 24: Parametrization of the VUV light using a landau + exponential function. Evolution with the distance
 518 of the model parameters.

519 An extra component from the reemitted visible light will be present in the configurations
 520 with TPB coated reflector foils. For the case of the geometry with foils covering only the
 521 cathode, the selected model was the same than for the VUV light. Fig. 25 shows the results.
 522 Similar degree of correlation than with the direct component is observed in all the parameters.
 523 To guide the eye better, in the panel showing the landau width where a poorer correlation
 524 is observed, the profile of the points is also shown following the density of the points (in
 525 magenta).

526 The visible light in the LDS with reflector foils covering all the active volume was more
 527 complicated. As Fig. 26 shows, two different populations are clearly distinguishable. They
 528 are related with the relative position of the scintillation points to the foils. To separate both
 populations we have used the relation between t_0 and the average of the path lengths (in ns)
 from the shortest reflection off each of the foils ($t_{geometry}$) shown in Fig. 27.

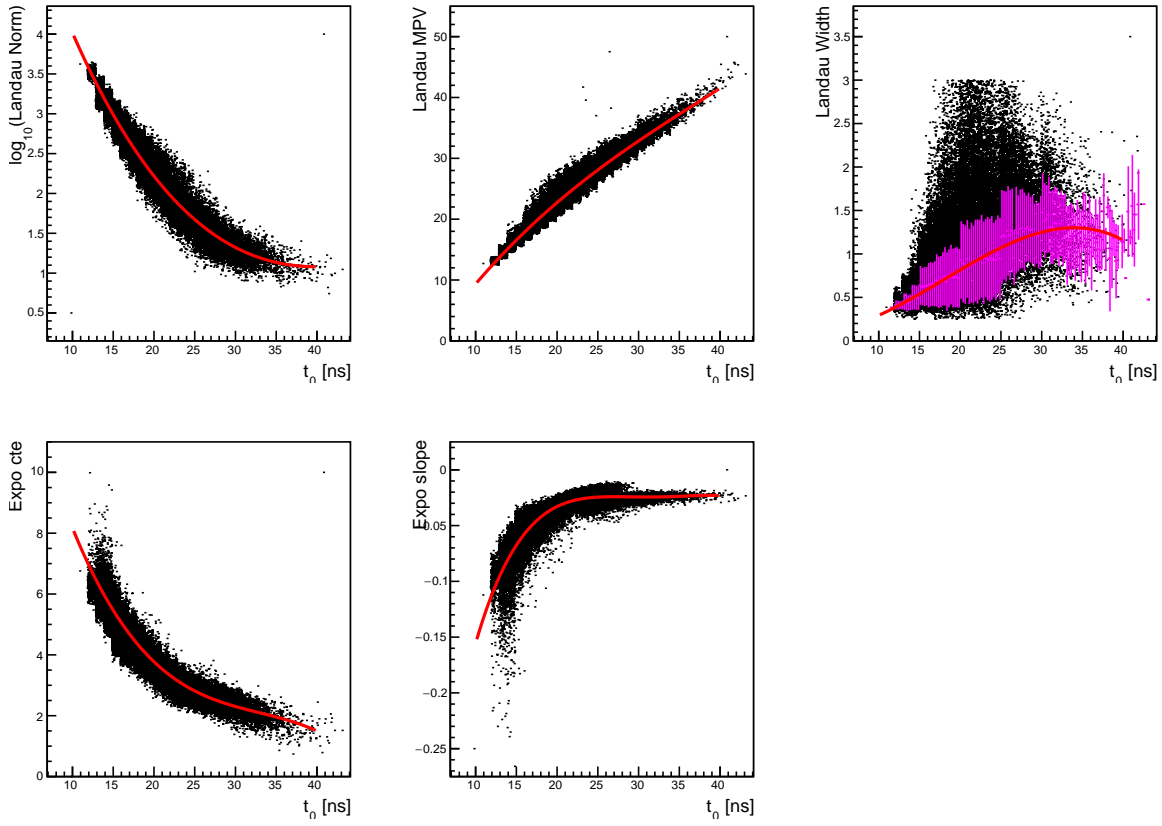


Figure 25: Parametrization of the visible light using a landau + exponential function for the “cathode only” configuration. Evolution with t_0 of the model parameters.

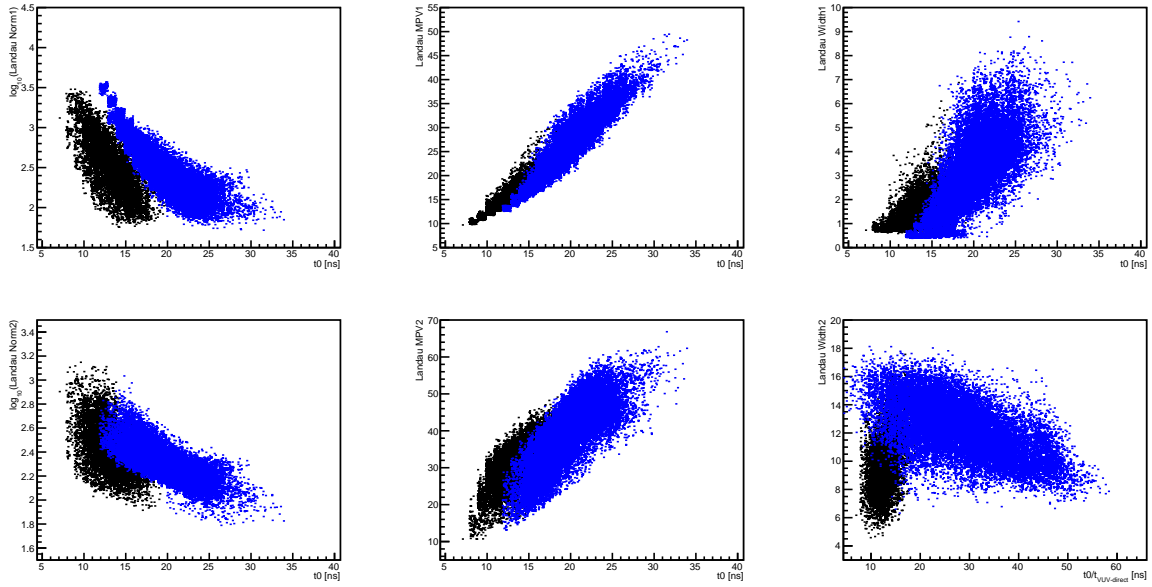


Figure 26: Parametrization of the visible light using a landau + landau function for the “full coverage” configuration. Evolution with t_0 of the model parameters. Note that the width of the second landau in the “population 2” has been parametrized as a fuction of the time $t_{VUV\text{-}direct}$ instead of t_0 , to increase the degree of correlation.

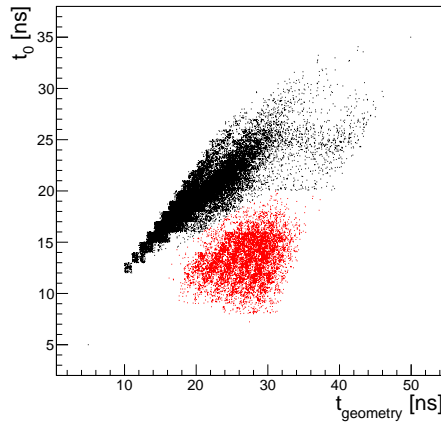


Figure 27: t_0 and $t_{geometry}$ scatter plot used for the separation of the two populations found in the parametrizations of the “full coverage” configuration model. Each color represents one population.

529 After been able to separate between the two populations, Figs. 28 and 29 show the
 530 correlation between the six parameters of the landau + landau model used in this case with
 531 the minimum time of flight.

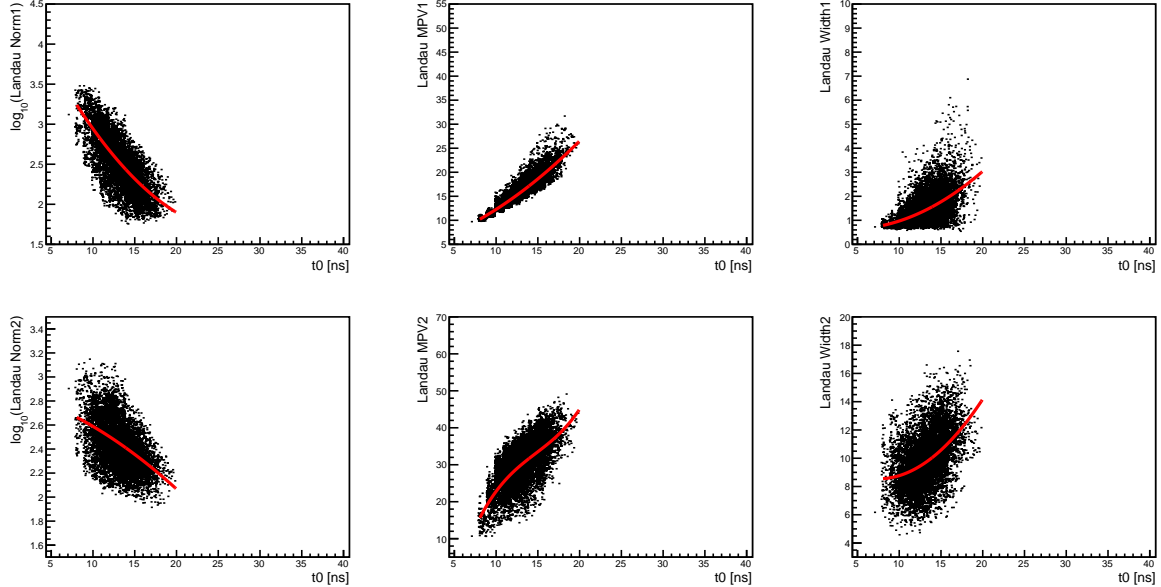


Figure 28: Parametrization of the visible light using a landau + landau function for the “full coverage” configuration. Evolution of the model parameters for the so-called ”population 1”.

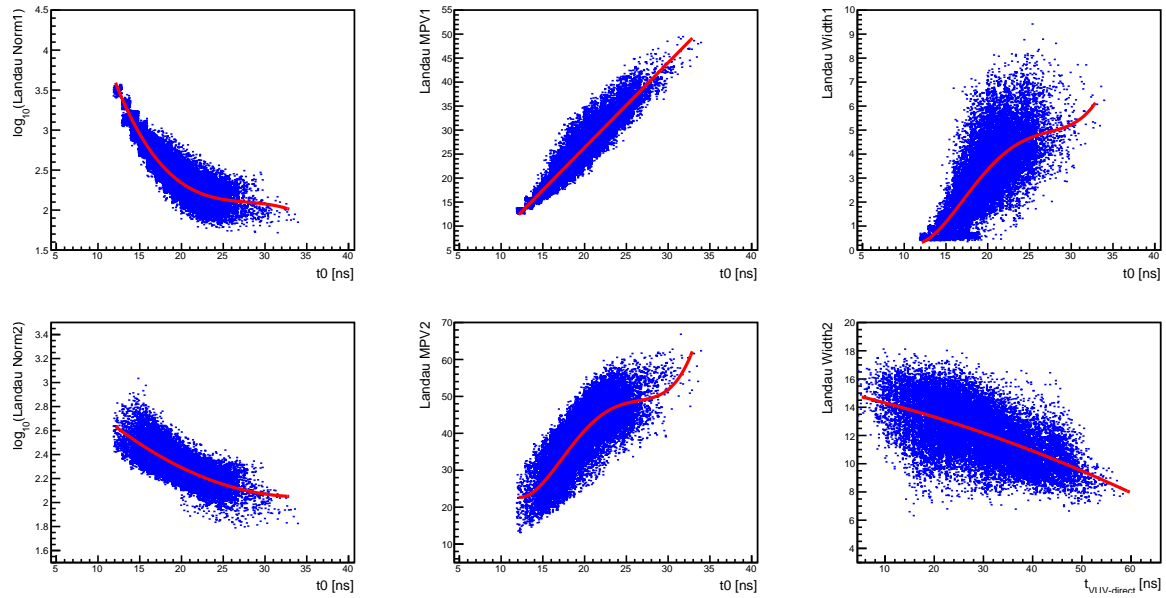


Figure 29: Parametrization of the visible light using a landau + landau function for the “full coverage” configuration. Evolution of the model parameters for the so-called ”population 2”.

B Timing Resolution Plots

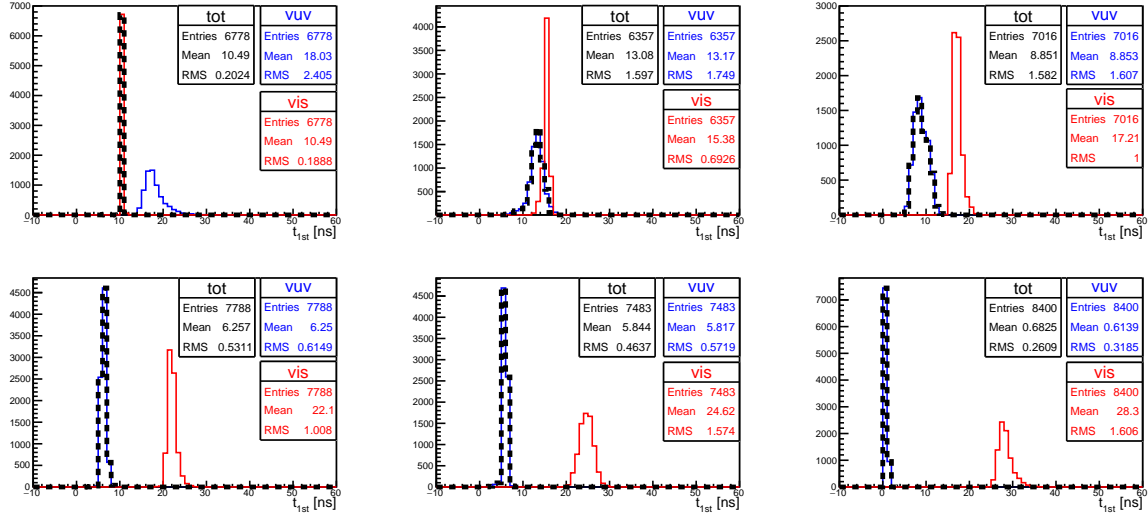


Figure 30: Distributions of the first arrival times for proton events simulated with energies between 20 and 500 MeV, for the different components VUV (blue), visible (red) and total (black), in the configuration with an opaque cathode covered by TPB-coated reflector foils. All the protons were injected in the center of the TPC, $(y, z) = (0, 250 \text{ cm})$, at different distances to the photocathode plane $\langle x \rangle = 205, 165, 125, 85, 70 and 35 cm from left to right - top to bottom.$

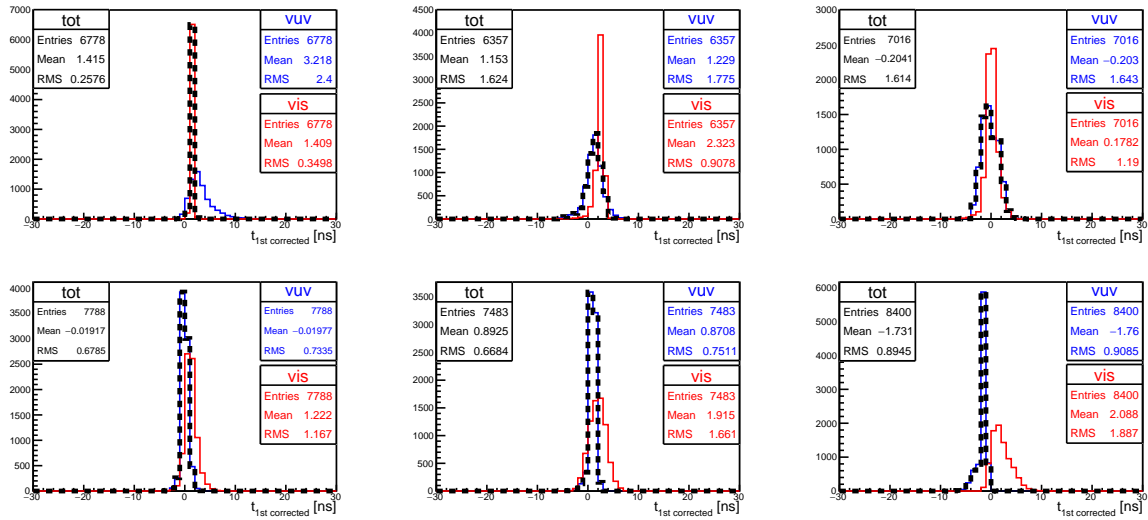


Figure 31: Distributions of the reconstructed times of the events shown in Figure 30.

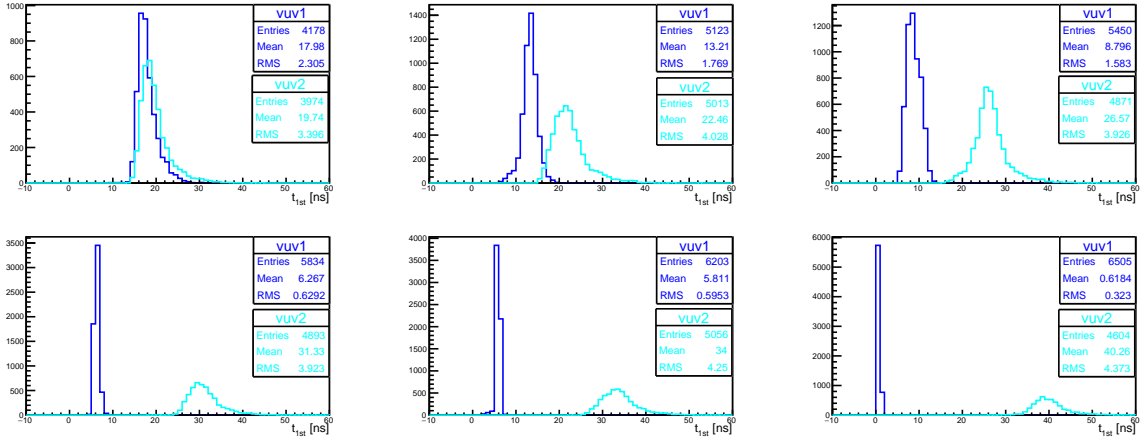


Figure 32: Distributions of the first arrival times for proton events simulated with energies between 20 and 500 MeV, for the VUV component in the TPC where the scintillation is happening (blue) and the VUV component seen by the LDS in the TPC after a cathode with a 70% transparency. All the protons were injected in the center of one TPC, $(y, z) = (0, 250 \text{ cm})$, at different distances to its photocathode plane $\langle x \rangle = 205, 165, 125, 85, 70$ and 35 cm from left to right - top to bottom. All these $\langle x \rangle$ values are 200 cm larger for the case of the TPC after the 70% transparent cathode.

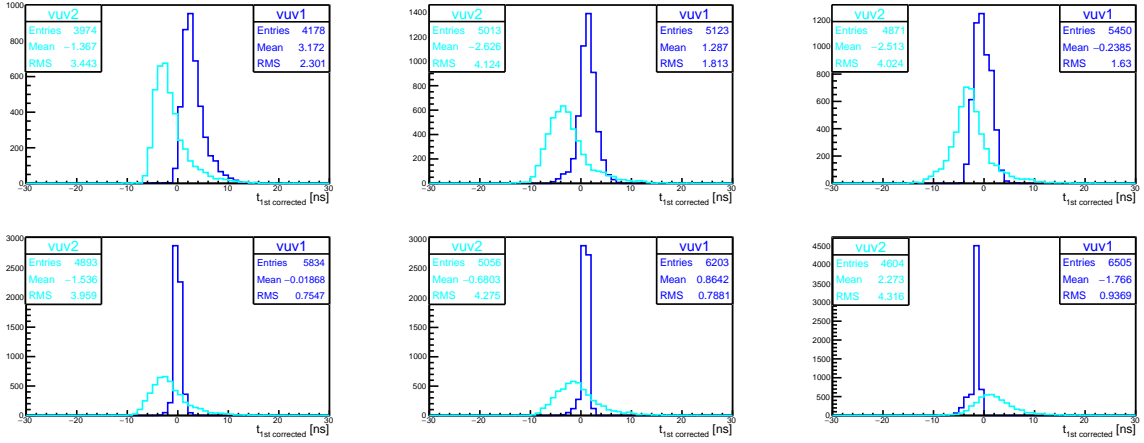


Figure 33: Distributions of the reconstructed times of the events shown in Figure 32.

C Energy Resolution Plots

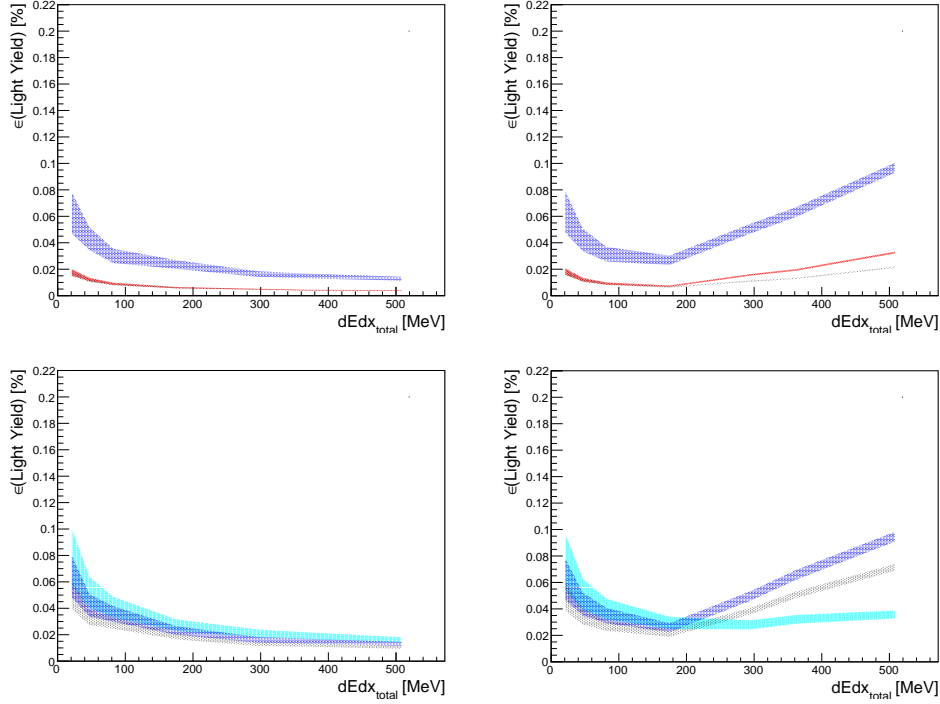


Figure 34: Relative uncertainty of the detected light yield as a function of the energy deposited in the LAr active volume for a sample of protons injected close to the center of the TPC (5 cm, 0, 250 cm) in the beam direction.

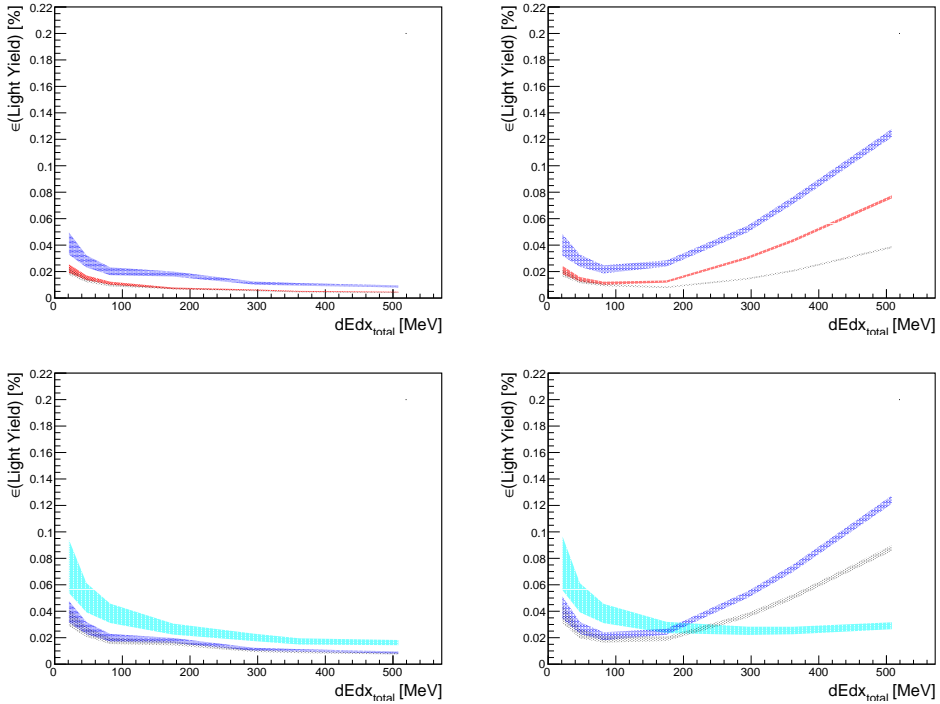


Figure 35: Relative uncertainty of the detected light yield as a function of the energy deposited in the LAr active volume for a sample of protons injected close to the center of the TPC (45 cm, 0, 250 cm) in the beam direction.

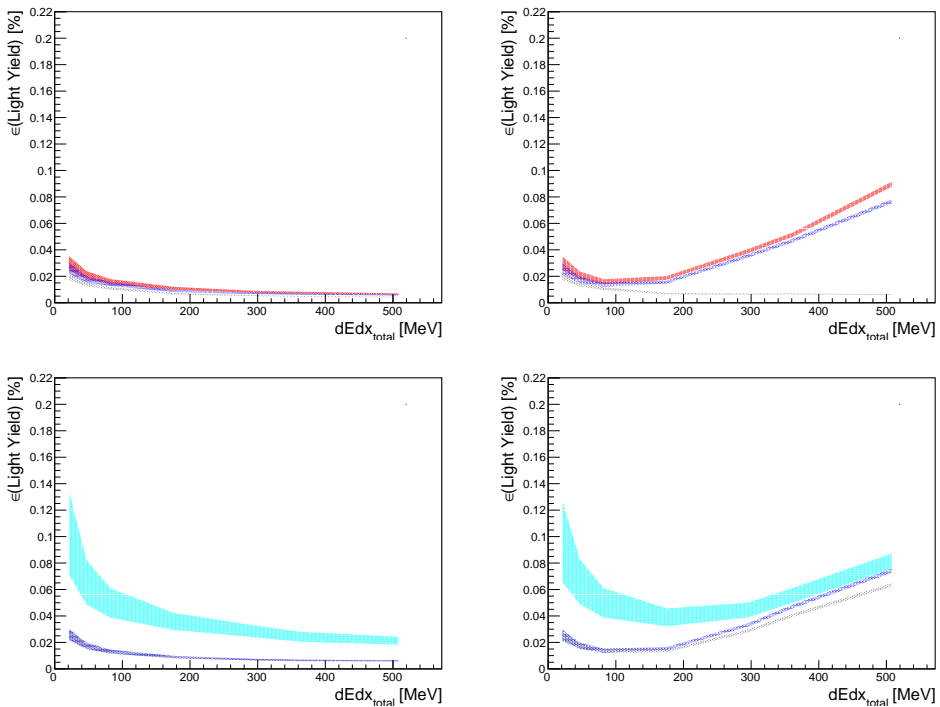


Figure 36: Relative uncertainty of the detected light yield as a function of the energy deposited in the LAr active volume for a sample of protons injected close to the center of the TPC (125 cm, 0, 250 cm) in the beam direction.

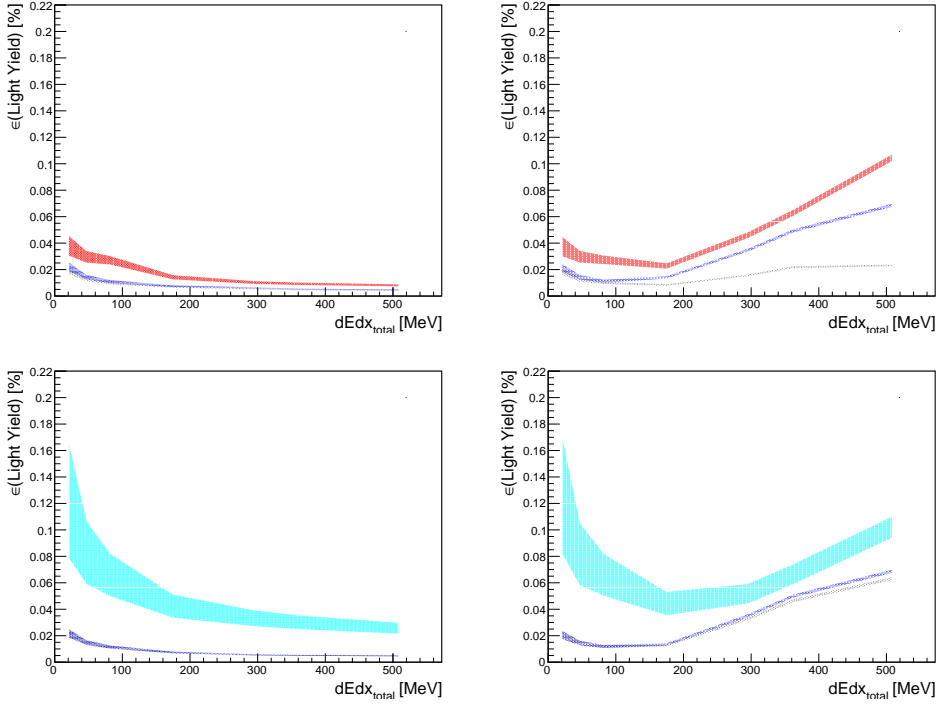


Figure 37: Relative uncertainty of the detected light yield as a function of the energy deposited in the LAr active volume for a sample of protons injected close to the center of the TPC (145 cm, 0, 250 cm) in the beam direction.

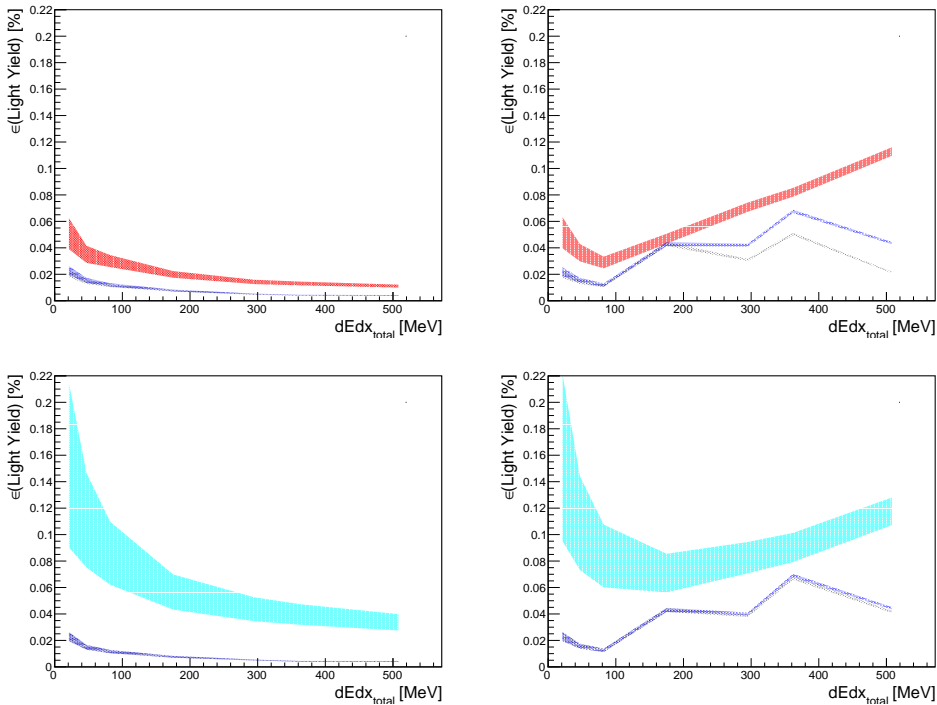


Figure 38: Relative uncertainty of the detected light yield as a function of the energy deposited in the LAr active volume for a sample of protons injected close to the center of the TPC (185 cm, 0, 250 cm) in the beam direction.

D Position Resolution Plots

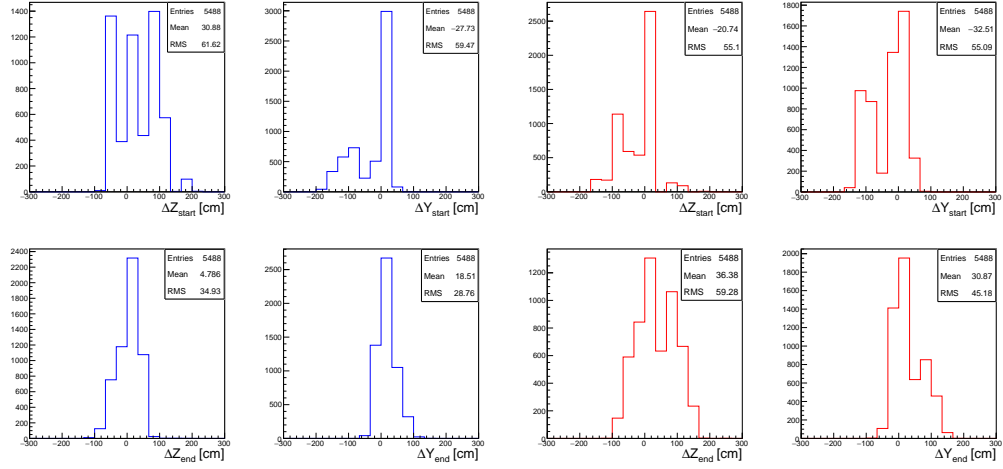


Figure 39: Resolution in the estimation of the (z, y) *start* (top) and *end* (bottom) points, using the VUV (left) and the visible (right) light components, for a sample of cosmics (~ 1 GeV muons) with different topologies (see Figure 20).

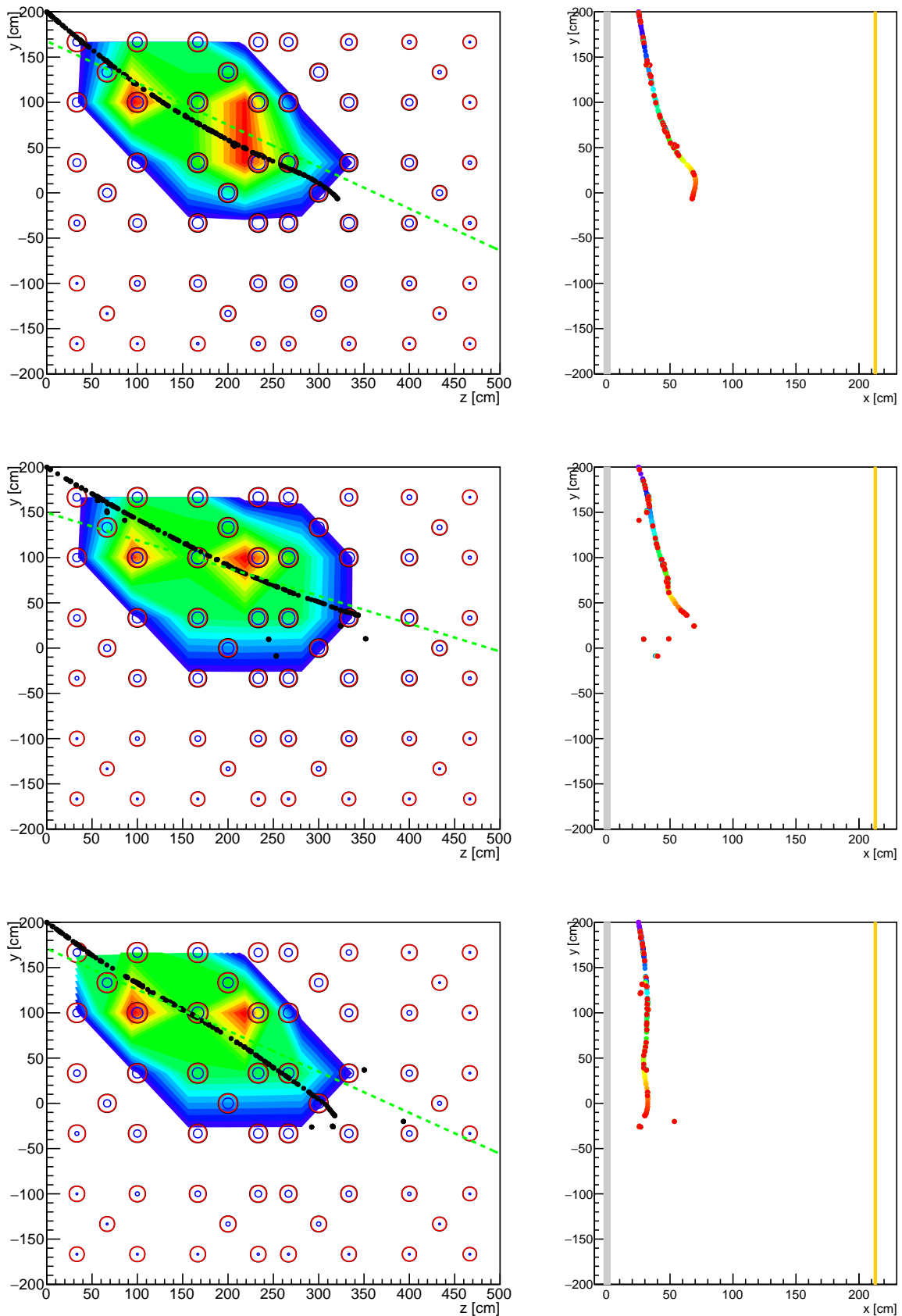


Figure 40: Examples of *cosmic* tracking using the light.

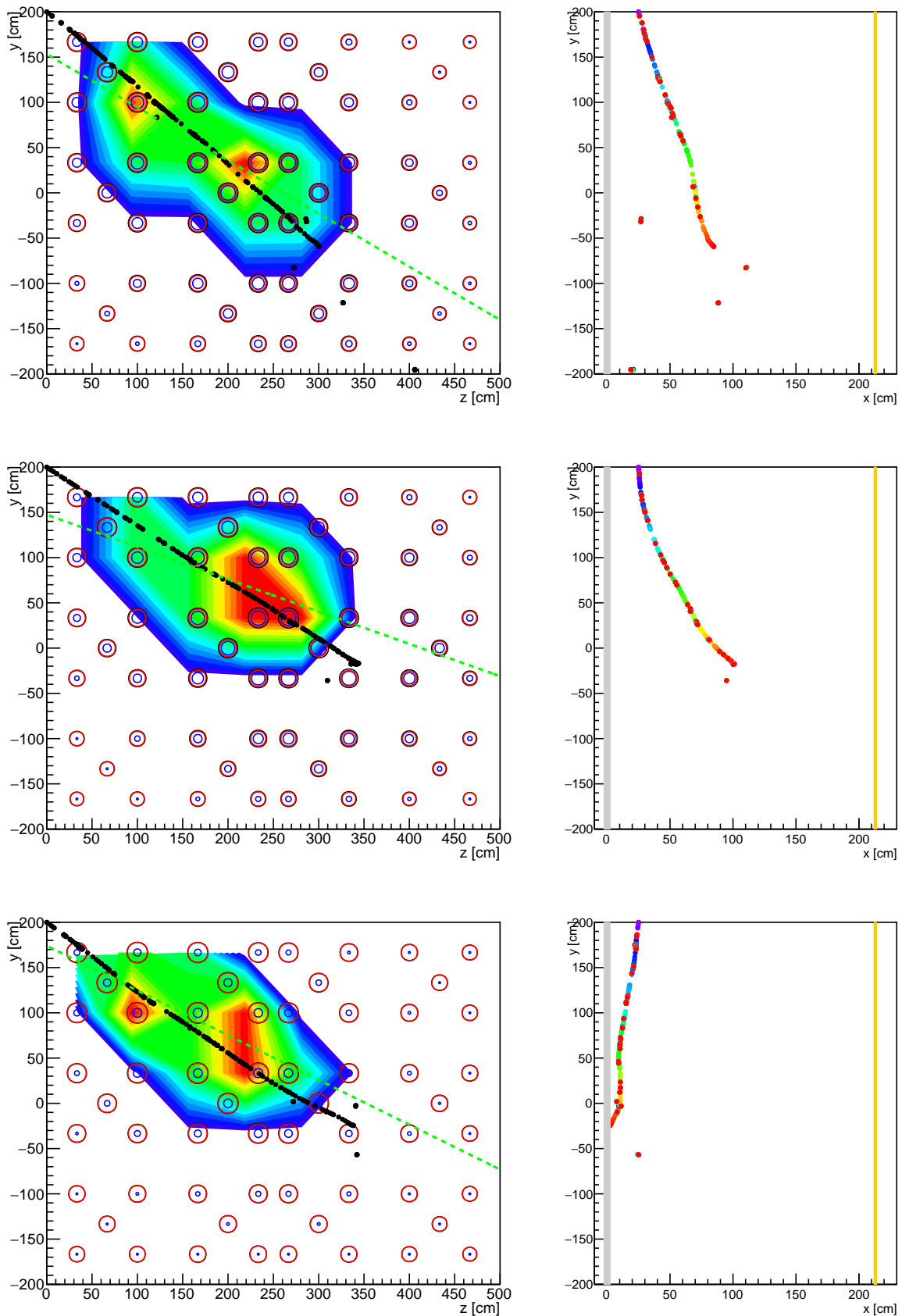


Figure 41: Examples of *cosmic* tracking using the light.

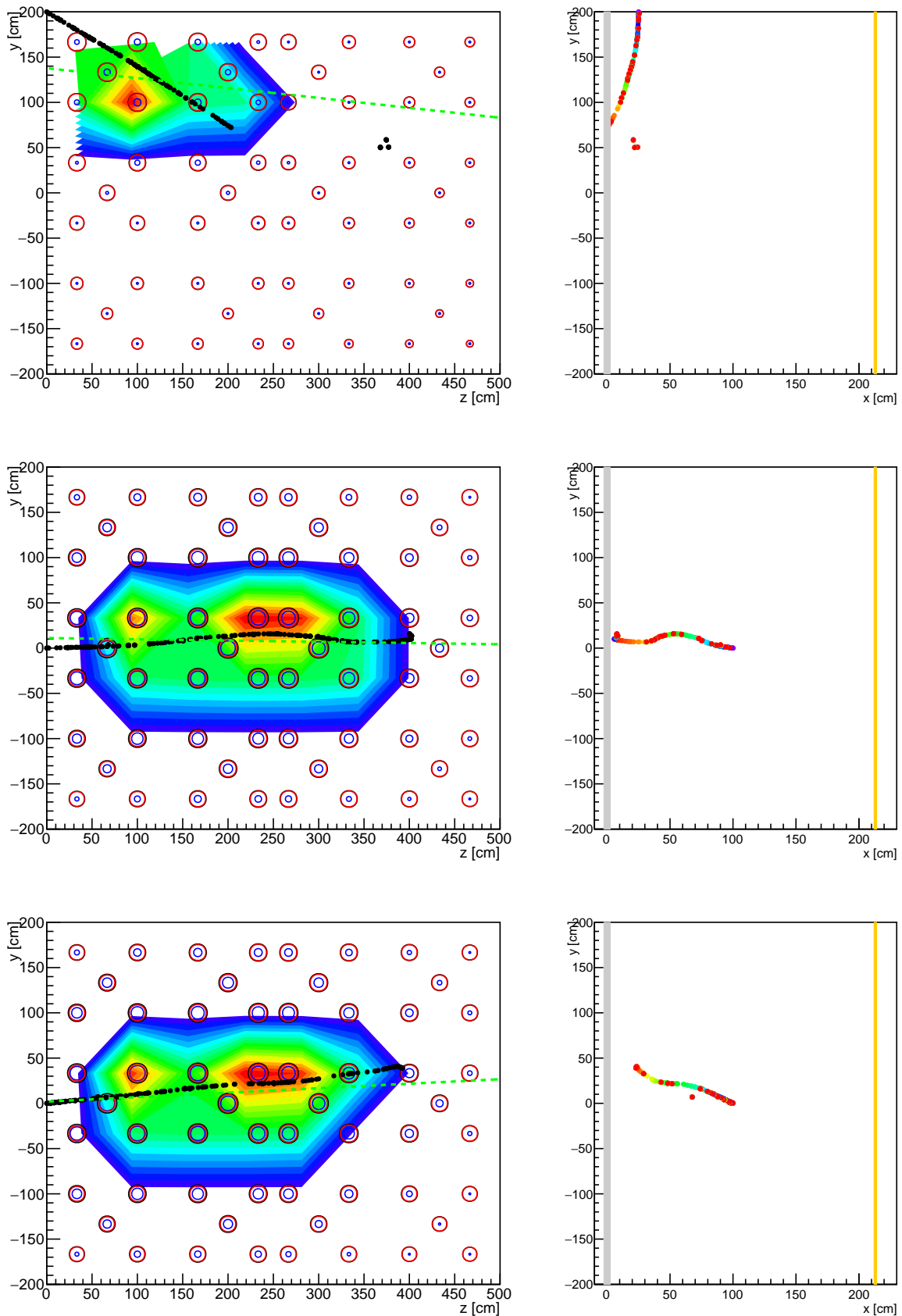


Figure 42: Examples of *cosmic* tracking using the light.

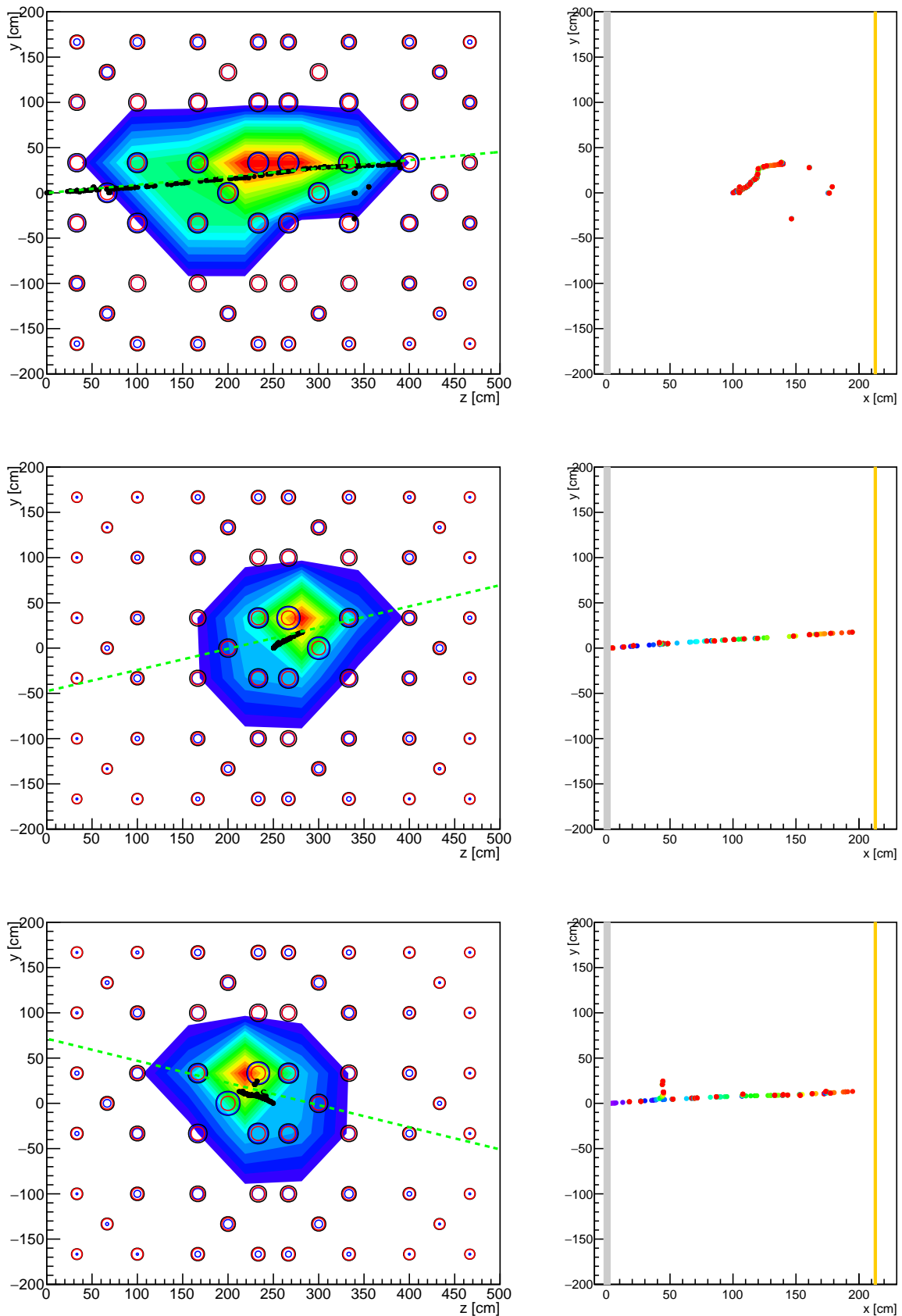


Figure 43: Examples of *cosmic* tracking using the light.

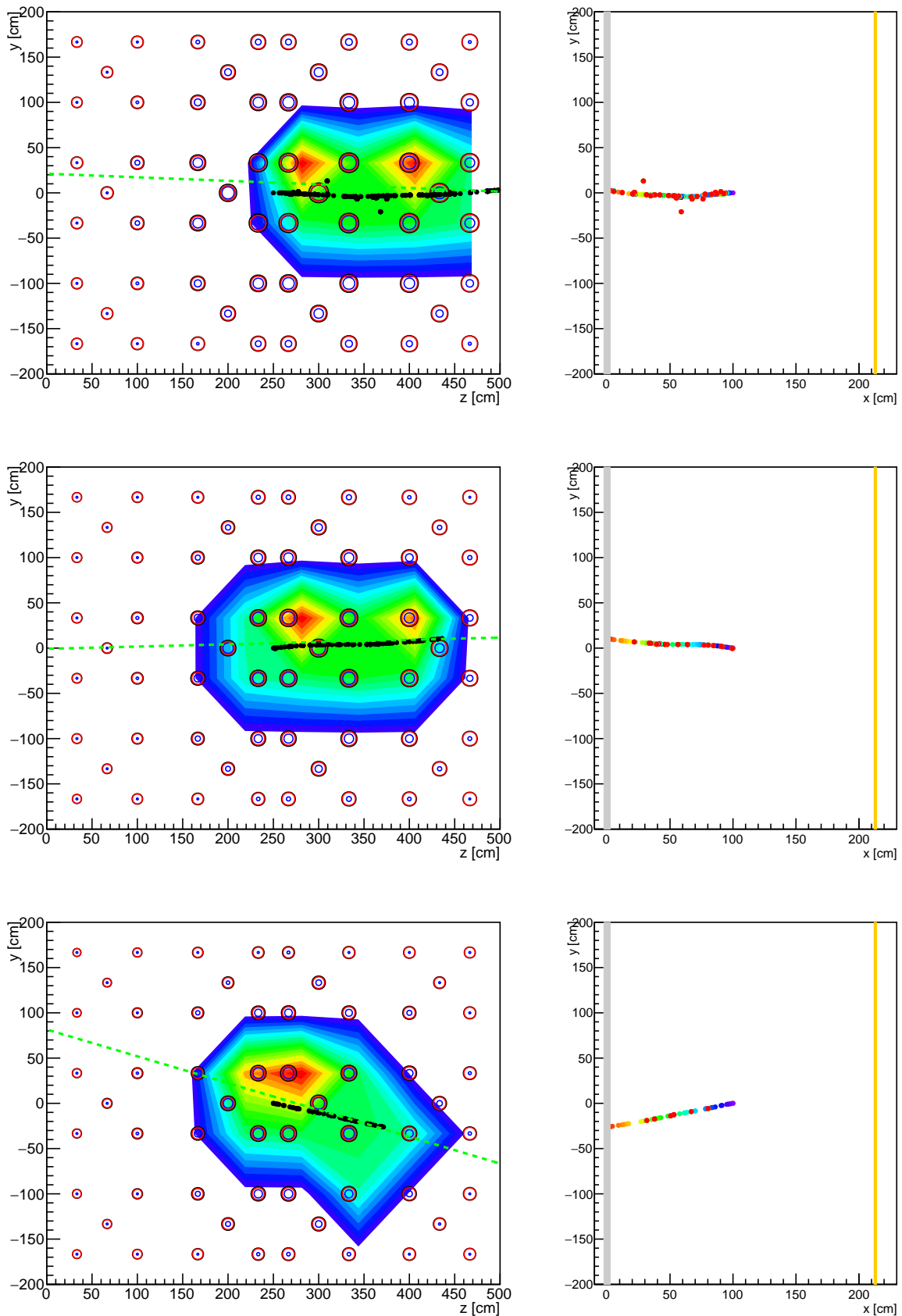


Figure 44: Examples of *cosmic* tracking using the light.

535 **References**

- [1] E. Segreto, *Evidence of delayed light emission of tetraphenyl-butadiene excited by liquid-argon scintillation light*, *Phys. Rev.* **C 91**, 035503.
- [2] P. Benetti et al., *First results from a Dark Matter search with liquid Argon at 87 K in the Gran Sasso Underground Laboratory*, *Astropart. Phys.* **28** (2008) 495.
R. Acciarri et al., *Demonstration and comparison of photomultiplier tubes at liquid Argon temperature*, *JINST* **7** (2012) P01016.
- [3] P. Agnes et al., *First Results from the DarkSide-50 Dark Matter Experiment at Laboratori Nazionali del Gran Sasso*, *Physics Letters B* 743, 456 (2015).
- [4] R. Acciarri et al., *A study of electron recombination using highly ionizing particles in the ArgoNeuT Liquid Argon TPC*, *JINST* **8** (2013) P08005.
- [5] T. Doke, *Fundamental properties of liquid Argon, Krypton and Xenon as Radiation detector media*, *Portgal Phys* **12** (1981) 9.
- [6] R. Acciarri et al., *A Proposal for a Three Detector Short-Baseline Neutrino Oscillation Program in the Fermilab Booster Neutrino Beam*, *arXiv:1503.01520 [physics.ins-det]* (2015).
- [7] M. Sorel, *Expected performance of an ideal liquid argon neutrino detector with enhanced sensitivity to scintillation light* , *JINST* **9** (2014) 10002.
- [8] S. Amerio et al., *Design, construction and tests of the ICARUS T600 detector*, *NIM* **527** (2004) 329-410.
- [9] R. Acciarri et al., *LArIAT: Liquid Argon In A Testbeam*, *arXiv:1406.5560 [physics.ins-det]* (2014).
- [10] MicroBooNE detector paper, in preparation.
- [11] Colton Hill studies. Technical Note in preparation.
- [12] E. Baller et al., *Liquid Argon Time Projection Chamber research and development in the United States* , *JINST* **9** (2014) T05005.
- [13] T. Heindl et al., *The scintillation of liquid argon*, *JEPL* **91** (2010) 62002.